6 Kinetics

There are three distinct events in the evolution of bainite (Fig. 6.1). A sub-unit nucleates at an austenite grain boundary and lengthens until its growth is arrested by plastic deformation within the austenite. New sub-units then nucleate at its tip, and the sheaf structure develops as this process continues. The average lengthening rate of a sheaf must be smaller than that of a sub-unit because of the delay between successive sub-units. The volume fraction of bainite depends on the totality of sheaves growing from different regions in the sample. Carbide precipitation influences the reaction rate by removing carbon either from the residual austenite or from the supersaturated ferrite.
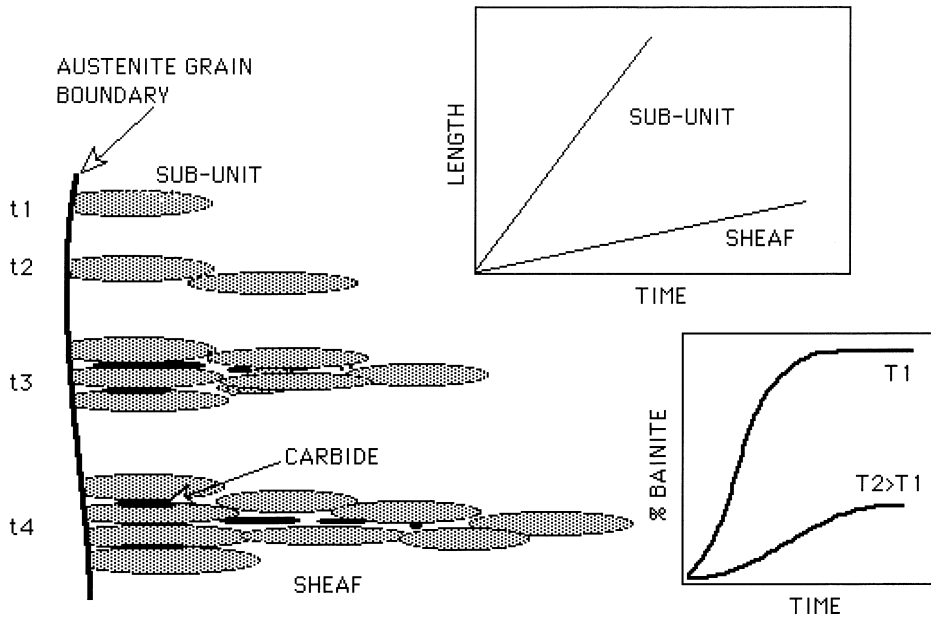

Fig. 6.1 The microstructural features relevant in the kinetic description of a bainitic microstructure. There is the lengthening of sub-units and of sheaves, the latter by the repeated nucleation of sub-units, the precipitation of carbides, and the change in volume fraction as a function of time and temperature.

129

6.1 Thermodynamics of Nucleation

It was shown in Chapter 5 that the equilibrium compositions $x^{\alpha\gamma}$ and $x^{\gamma\alpha}$ of ferrite and austenite respectively, are obtained using the common tangent construction. The same construction can be used to determine the change in free energy $\Delta G^{\gamma \rightarrow \gamma' + \alpha}$ when austenite of composition $\bar{x}$ decomposes into the equilibrium mixture of ferrite and carbon-enriched austenite (γ'), Fig. 6.2a.
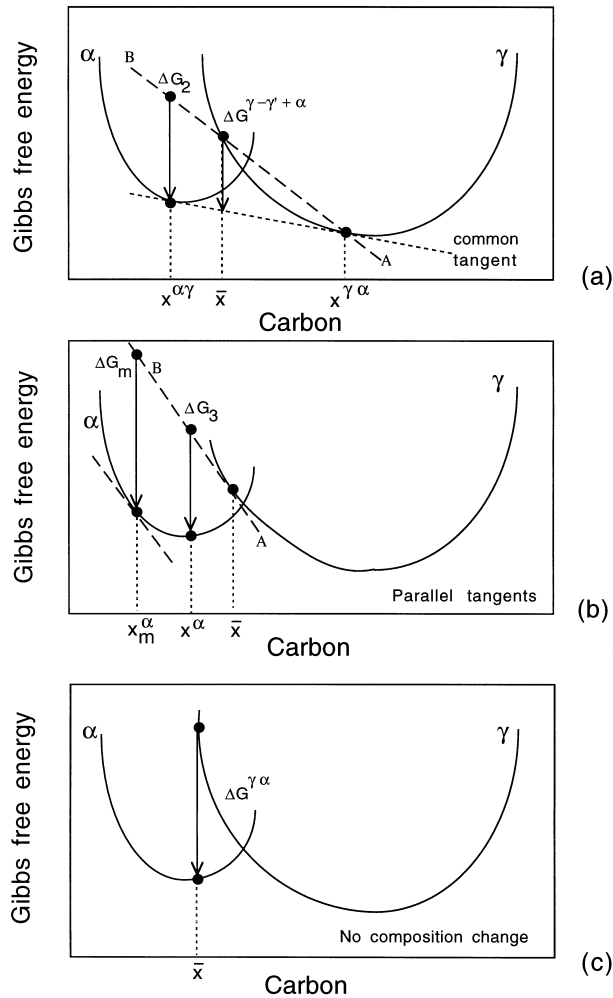

Fig. 6.2 Free energy diagrams illustrating the chemical free energy changes during the nucleation and growth of ferrite from austenite of composition $\bar{x}$. The term γ' refers to austenite which is enriched in carbon as a result of the decomposition of austenite of composition $\bar{x}$ into a mixture of ferrite and austenite.

130

The equilibrium fraction of ferrite is given by the lever rule as $(x^{\gamma\alpha} - \overline{x})/$ $(x^{\gamma\alpha} - x^{\alpha\gamma})$. It follows that the free energy change per mole of ferrite is

$$\Delta G_2 = \Delta G^{\gamma \rightarrow \gamma' + \alpha} \times \frac{x^{\gamma\alpha} - x^{\alpha\gamma}}{x^{\gamma\alpha} - \overline{x}}$$

(Fig. 6.2a).

There is a significant change in the chemical composition of the austenite when it changes into the equilibrium mixture of ferrite and austenite. A ferrite nucleus on the other hand has such a small volume that it hardly affects the composition of the remaining austenite. The calculation of the free energy change associated with nucleation must therefore take into account that only a minute quantity of ferrite is formed. Consider the change ΔG_2 as austenite decomposes to a mixture of ferrite and enriched austenite of composition $x^{\gamma} = x^{\gamma\alpha}$. As the fraction of ferrite is reduced, x^{γ} and $\overline{x}$ move towards each other causing the line AB to tilt upwards. In the limit that $x^{\gamma} = \overline{x}$, AB becomes tangential to the curve at $\overline{x}$. The free energy change for the formation of a mole of ferrite nuclei of composition x^{α} is then given by ΔG_3, Fig. 6.2b.

The greatest reduction in free energy during nucleation is obtained if the composition of the ferrite nucleus is set to a value x_m, given by a tangent to the ferrite free energy curve which is parallel to the tangent to the austenite free energy curve at $\overline{x}$, as shown in Fig. 6.2b. This maximum possible free energy change for nucleation is designated ΔG_m.

There is simplification when the transformation occurs without composition change (Fig. 6.2c). The change $\Delta G^{\gamma \rightarrow \alpha}$ is the vertical distance between the austenite and ferrite free energy curves at the composition of interest.

6.1.1 Transformation-Start Temperature

It is a common observation that the Widmanstätten ferrite-start (W_S) and bainite-start (B_S) temperatures are more sensitive to the steel composition than is the Ae_3 temperature. This indicates that the influence of solutes on the nucleation of Widmanstätten ferrite and bainite is more than just thermodynamic (Fig. 6.3a).

Some clues to this behaviour come from studies of time-temperature-transformation diagrams, which consist essentially of two C-curves. The lower C-curve has a characteristic flat top at a temperature T_h, which is the highest temperature at which ferrite can form by displacive transformation (Fig. 6.3b). The transformation product at T_h may be Widmanstätten ferrite or bainite.

The driving force ΔG_m available for nucleation at T_h, is plotted in Fig. 6.4a, where each point comes from a different steel. The transformation product at T_h can be Widmanstätten ferrite or bainite, but it is found that there is no need to distinguish between these phases for the purposes of nucleation. The same
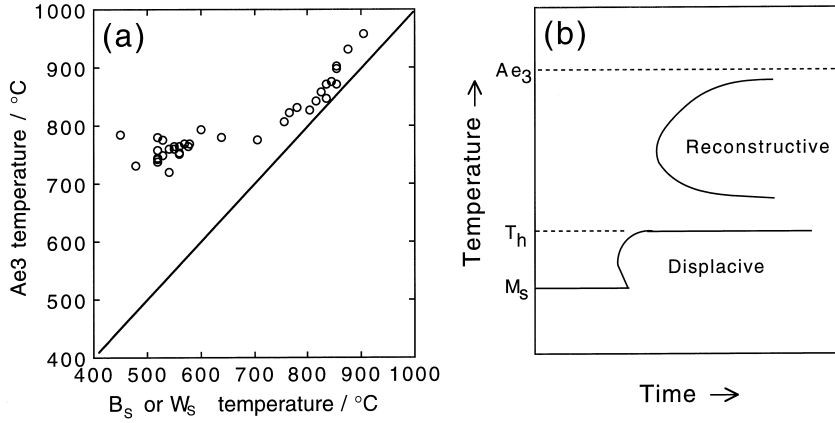
Fig. 6.3 (a) The variation of the Widmanstätten ferrite-start and bainite-start temperatures as a function of the Ae_3 temperature of the steel concerned (Ali, 1990). (b) Schematic TTT diagram illustrating the two C-curves and the T_h temperature.

nucleus can develop into either phase depending on the prevailing thermodynamic conditions. The analysis proves that carbon must partition during the nucleation stage in order always to obtain a reduction in free energy. The situation illustrated in Fig. 6.4b is not viable since diffusionless nucleation would in some cases lead to an increase in the free energy.

The plots in Fig. 6.4 are generated using data from diverse steels. Figure 6.4a represents the free energy change ΔG_m at the temperature T_h where displacive transformation first occurs. The free energy change can be calculated from readily available thermodynamic data. It follows that Fig. 6.4a can be used to estimate T_h for any steel. The equation fitted to the data in Fig. 6.4a is (Ali and Bhadeshia, 1990):

$$G_N = C_1(T - 273.18) - C_2 \qquad \text{J mol}^{-1} \tag{6.1}$$

where the fitting constants are found to be $C_1 = 3.637 \pm 0.2 \, \text{J mol}^{-1} \text{K}^{-1}$ and $C_2 = 2540 \pm 120 \, \text{J mol}^{-1}$ for the temperature range 670–920 K. G_N is to be regarded as a *universal nucleation function*, because it defines the minimum driving force necessary to achieve a perceptible nucleation rate for Widmanstätten ferrite or bainite in any steel.

6.1.2 Evolution of the Nucleus

The nucleus is identical for Widmanstätten ferrite and for bainite; it must therefore be growth which distinguishes them. But what determines whether the nucleus evolves into bainite or Widmänsstatten ferrite?
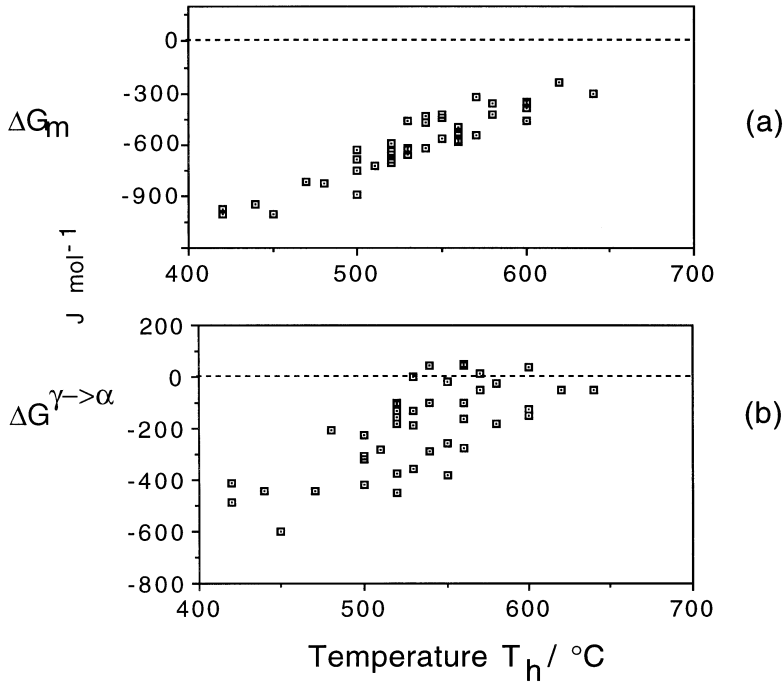
Fig. 6.4 The free energy change necessary in order to obtain a detectable degree of transformation. Each point represents a different steel and there is no distinction made between Widmanstätten ferrite or bainite. (a) Calculated assuming the partitioning of carbon during nucleation. (b) Calculated assuming that there is no change in composition during nucleation. After Bhadeshia, 1981a.

The answer is straightforward. If diffusionless growth cannot be sustained at T_h then the nucleus develops into Widmanstätten ferrite so that T_h is identified with W_S. A larger undercooling is necessary before bainite can be stimulated. If, however, the driving force at T_h is sufficient to account for diffusionless growth, then $T_h = B_S$ and Widmanstätten ferrite does not form at all.

It follows that Widmänsstatten ferrite forms below the Ae_3 temperature when:

$$\Delta G^{\gamma \rightarrow \gamma' + \alpha} < -G_{SW}$$
$$\Delta G_m < G_N$$

(6.2)

where G_{SW} is the stored energy of Widmanstätten ferrite (about 50 $J\,mol^{-1}$). The first of these conditions ensures that the chemical free energy change exceeds the stored energy of the Widmanstätten ferrite, and the second that there is a detectable nucleation rate.

133

Bainite is expected below the T_0' temperature when:

$$\Delta G^{\gamma \to \alpha} < -G_{SB} \tag{6.3}$$

$$\Delta G_m < G_N \tag{6.4}$$

where G_{SB} is the stored energy of bainite (about $400\,\mathrm{J\,mol^{-1}}$). The universal function, when used with these conditions, allows the calculation of the Widmanstätten ferrite-start and bainite-start temperatures from a knowledge of thermodynamics alone.

In this scheme, carbon is partitioned during nucleation but in the case of bainite, not during growth which is diffusionless. There is no inconsistency in this concept since a greater fraction of the free energy becomes available as the particle surface to volume ratio, and hence the influence of interfacial energy, decreases. The theory explains why both Widmanstätten ferrite and bainite can form during the early stages of isothermal transformation at temperatures close to B_S (Chang, 1999).

The scheme is illustrated in Fig. 6.5 which incorporates an additional function $G_N^{\alpha'}$ representing the critical driving force $\Delta G^{\gamma \to \alpha}\{M_S\}$ needed to stimulate martensite by an athermal, diffusionless nucleation and growth mechanism. Whereas it is reasonable to set $G_N^{\alpha'}$ to a constant value for low alloy steels
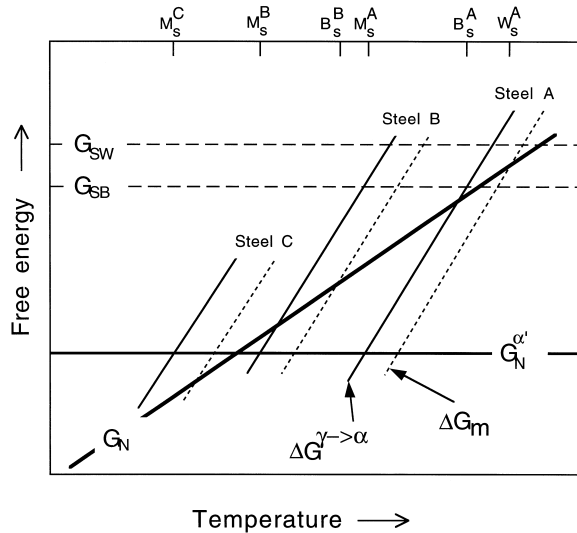

Fig. 6.5 Free energy curves for a low (*A*), medium (*B*) and high (*C*) alloy steel showing the conditions necessary for the nucleation and growth of Widmanstätten ferrite, bainite and martensite.

134

(Bhadeshia, 1981c,d) a function dependent on the strength of the austenite has to be used for steels containing large concentrations of solute (Ghosh and Olson, 1994).

The three common displacive transformations in steels include Widmanstätten ferrite, bainite and martensite. It is intriguing that they are not all found in every steel. Only martensite occurs in Fe–28Ni–0.4C wt%, whereas only bainite and martensite are found in Fe–4Cr–0.3C wt%. This is readily explained: steels *A*, *B* and *C* in Fig. 6.5 contain increasing quantities of austenite stabilising elements, with the driving force for transformation decreasing as the alloy content increases. In steel *A*, all three transformations are expected in turn as the temperature is reduced. For steel *B*, the temperature at which Widmanstätten ferrite nucleation becomes possible also corresponds to that at which bainite can grow. Bainite has a kinetic advantage so Widmanstätten ferrite does not form. Further alloying increases the stability of the austenite so much that the nucleation of Widmanstätten ferrite and bainite is suppressed to temperatures below M_S in which case they do not form at all.

The nucleation condition for bainite (eq. 6.4) becomes redundant for any steel in which Widmanstätten ferrite precedes bainite because they have a common nucleation mechanism.

An interesting prediction emerges from this rationale. For some steels the thermodynamic characteristics are such that the ΔG_m curve intersects the G_N function at two points, Fig. 6.6a (Bhadeshia and Svensson, 1989c). Widmanstätten ferrite then occurs at high temperatures, there is an intermediate temperature range where neither Widmanstätten ferrite nor bainite can nucleate, until bainite formation becomes possible at a lower temperature. The lower *C*-curve thus splits into two segments, one for Widmanstätten ferrite and a lower temperature segment for bainite (Fig. 6.6b). This prediction from theory has been confirmed experimentally (Ali and Bhadeshia, 1991).

Finally, because G_N decreases linearly with T_h, it is expected that the W_S and B_S temperatures are depressed to a greater extent by solute additions than the Ae_3 temperature. A larger driving force is needed to achieve a given rate of nucleation when the transformation is depressed to lower temperatures by alloying. A justification for the form of the universal nucleation function G_N is given in the next section.

6.2   Possible Mechanisms of Nucleation

Phase fluctuations occur as random events due to the thermal vibration of atoms. An individual fluctuation may or may not be associated with a reduction in free energy, but it can only survive and grow if there is a reduction. There is a cost associated with the creation of a new phase, the interface energy,

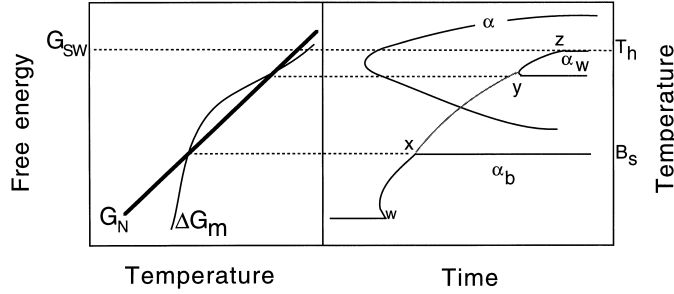**Fig. 6.6** (a) Free energy curves for the nucleation of Widmanstätten ferrite and bainite in a low alloy steel for which the ΔG_m and G_N curves exhibit a double intersection. (b) Calculated TTT diagram for the same steel, showing how Widmanstätten ferrite and bainite form separate C curves. The Widmanstätten ferrite and bainite C curves would ordinarily be just one curve, joined by the line *wxyz*. After Ali and Bhadeshia (1991).

a penalty which becomes smaller as the particle surface to volume ratio decreases. In a metastable system this leads to a critical size of fluctuation beyond which growth is favoured.

Consider the homogeneous nucleation of α from γ. For a spherical particle of radius r with an isotropic interfacial energy $\sigma_{\alpha\gamma}$, the change in free energy as a function of radius is:

$$\Delta G = \frac{4}{3}\pi r^3 \Delta G_{CHEM} + \frac{4}{3}\pi r^3 \Delta G_{STRAIN} + 4\pi r^2 \sigma_{\alpha\gamma} \qquad (6.5)$$

where $\Delta G_{CHEM} = G_V^\alpha - G_V^\gamma$, G_V is the Gibbs free energy per unit volume of α and G_{STRAIN} is the strain energy per unit volume of α. The variation in ΔG with size is illustrated in Fig. 6.7; the activation barrier and critical size obtained using equation 6.5 are given by:

$$G^* = \frac{16\pi\sigma_{\alpha\gamma}^3}{3(\Delta G_{CHEM} + \Delta G_{STRAIN})^2} \qquad \text{and} \qquad r^* = \frac{2\sigma_{\alpha\gamma}}{\Delta G_{CHEM} + \Delta G_{STRAIN}} \quad (6.6)$$

The important outcome is that in classical nucleation the activation energy varies inversely with the square of the driving force. And the mechanism involves random phase fluctuations. It is questionable whether this applies to cases where thermal activation is in short supply. In particular, an activation barrier must be very small indeed if the transformation is to occur at a proper rate at low temperatures.

One mechanism in which the barrier becomes sufficiently small involves the spontaneous dissociation of specific dislocation defects which are already present in the parent phase (Christian, 1951; Olson and Cohen, 1976). The disloca-
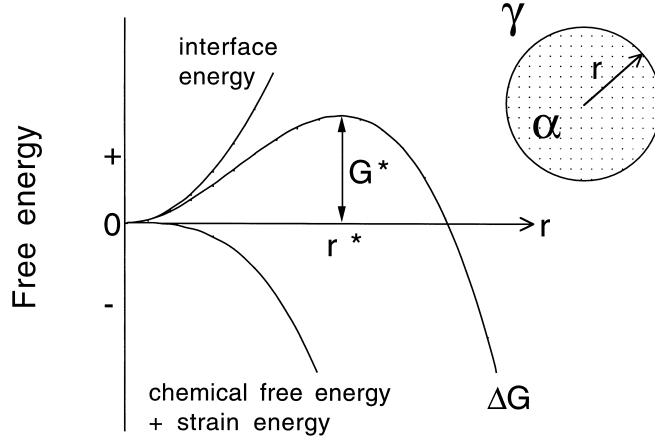
Fig. 6.7 The activation energy barrier G^* and the critical nucleus size r^* according to classical nucleation theory based on heterophase fluctuations.

tions are glissile so the mechanism does not require diffusion. The only barrier is the resistance to the glide of the dislocations. The nucleation event cannot occur until the undercooling is sufficient to support the faulting and strains associated with the dissociation process that leads to the creation of the new crystal structure (Fig. 6.8).

The free energy per unit area of fault plane is:

$$G_F = n_P \rho_A (\Delta G_{CHEM} + G_{STRAIN}) + 2\sigma_{\alpha\gamma}\{n_P\} \qquad (6.7)$$

where n_P is the number of close-packed planes participating in the faulting process, ρ_A is the spacing of the close-packed planes on which the faulting is assumed to occur. The fault energy can become negative when the austenite becomes metastable.

For a fault bounded by an array of n_P dislocations each with a Burger's vector of magnitude b, the force required to move a unit length of dislocation array is $n_P\tau_o b$. τ_o is the shear resistance of the lattice to the motion of the dislocations. G_F provides the opposing stress via the chemical free energy change ΔG_{CHEM}; the physical origin of this stress is the fault energy which becomes negative so that the partial dislocations bounding the fault are repelled. The defect becomes unstable, i.e. nucleation occurs, when

$$G_F = -n_P\tau_o b \qquad (6.8)$$

Take the energy barrier between adjacent equilibrium positions of a dislocation to be G_o^*. An applied shear stress τ has the effect of reducing the height of this barrier (Conrad, 1964; Dorn, 1968):
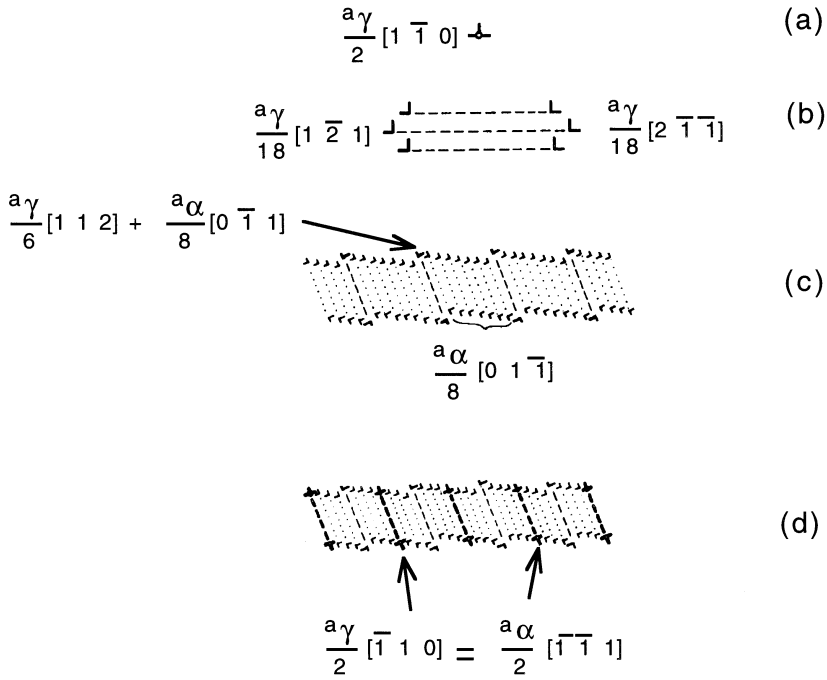
$$\frac{a_\gamma}{2}[1\ \bar{1}\ 0]\ \perp \qquad\qquad\qquad\qquad\text{(a)}$$

$$\frac{a_\gamma}{18}[1\ \bar{2}\ 1]\ \qquad\qquad\qquad \frac{a_\gamma}{18}[2\ \bar{1}\ \bar{1}] \qquad\text{(b)}$$

$$\frac{a_\gamma}{6}[1\ 1\ 2]\ +\ \frac{a_\alpha}{8}[0\ \bar{1}\ 1]$$

$$\frac{a_\alpha}{8}[0\ 1\ \bar{1}]$$

(c)

(d)

$$\frac{a_\gamma}{2}[\bar{1}\ 1\ 0]\ =\ \frac{a_\alpha}{2}[\bar{1}\ \bar{1}\ 1]$$

Fig. 6.8 Olson and Cohen model for the nucleation of α martensite. (a) Perfect screw dislocation in austenite. (b) Three-dimensional dissociation over a set of three close-packed planes. The faulted structure is not yet that of α. (c) Relaxation of fault to a body-centred cubic structure with the introduction of partial dislocations in the interface. (d) Addition of perfect screw dislocations which cancel the long range strain field of the partials introduced in (c).

$$G^* = G_o^* - (\tau - \tau_\mu)v^* \qquad\qquad\qquad (6.9)$$

where v^* is an activation volume and τ_μ is the temperature independent resistance to dislocation motion (Fig. 6.9). In the context of nucleation, the stress τ is not externally applied but comes from the chemical driving force. On combining the last three equations we obtain

$$G^* = G_o^* + \left[\tau_\mu + \frac{\rho_A}{b}G_{STRAIN} + \frac{2\sigma}{n_P b}\right]v^* + \frac{\rho_A v^*}{b}\Delta G_{CHEM} \qquad (6.10)$$

It follows that with this model of nucleation the activation energy G^* will decrease *linearly* as the magnitude of the driving force ΔG_{CHEM} increases. This direct proportionality contrasts with the inverse square relationship of classical theory.
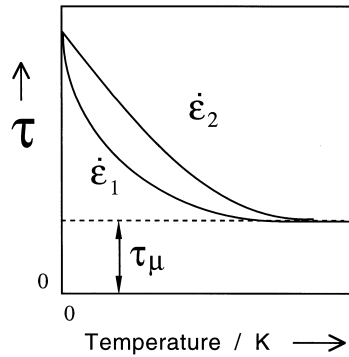
Fig. 6.9 Temperature dependence of the applied stress necessary to move a dislocation at two different strain rates ($\dot{\epsilon}_2 > \dot{\epsilon}_1$). τ_μ is the athermal resistance which never vanishes. After Conrad (1964).

6.3   Bainite Nucleation

The linear relationship between G_N and T_h (Fig. 6.4) can be used to deduce whether nucleation involves dislocation dissociation or heterophase fluctuations (Bhadeshia, 1981a). The nucleation rate I_V will have a temperature dependence due to the activation energy:

$$I_V \propto \nu \exp\{-G^*/RT\} \qquad (6.11)$$

where ν is an attempt frequency. It follows that

$$-G^* \propto \beta T \qquad \text{where} \qquad \beta = R \ln\{I_V/\nu\} \qquad (6.12)$$

We now assume that there is a specific nucleation rate at T_h, irrespective of the type of steel, in which case β is a constant, negative in value since the attempt frequency should be larger than the actual rate. This gives the interesting result that

$$G_N \propto \beta T \qquad (6.13)$$

which is precisely the relationship observed experimentally. This is evidence for nucleation by the dissociation of dislocations with the activation energy proportional to the driving force, as opposed to the inverse square relationship predicted by classical theory. The activation energy G^* in this model comes from the resistance of the lattice to the motion of dislocations.

Nucleation corresponds to a point where the slow, thermally activated migration of glissile partial dislocations gives way to rapid, breakaway dissociation. This is why it is possible to observe two sets of transformation units, the first consisting of very fine embryo platelets below the size of the operational nucleus, and the second the size corresponding to the rapid growth

to the final size. Intermediate sizes are rarely observed because the time period for the second stage is expected to be much smaller than that for the first. Figure 6.10 shows that in addition to the fully growth sub-units (a few micrometers in length), there is another population of much smaller (submicron) particles which represent the embryos at a point in their evolution prior to breakaway dissociation.

6.4   Empirical Equation for the Bainite-Start Temperature

Steven and Haynes (1956) measured the bainite-start temperature by isothermally transforming a large number of engineering steels with chemical composition in the range (wt%):

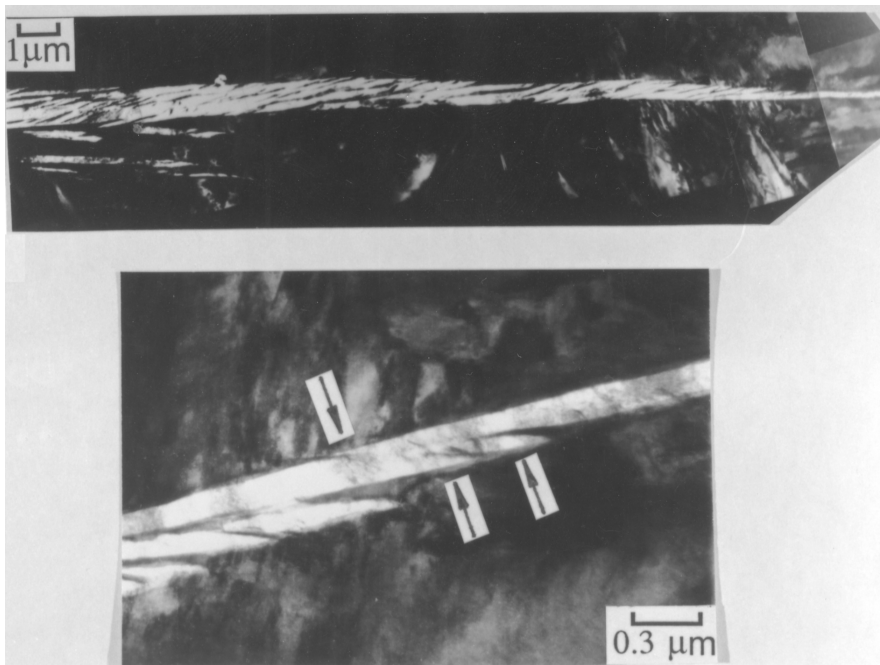|			
Carbon	0.1–0.55	Nickel	0.0–5.0
Silicon	0.1–0.35	Chromium	0.0–3.5
Manganese	0.2–1.7	Molybdenum	0.0–1.0

Fig. 6.10 Transmission electron micrograph of a sheaf of bainite in a partially transformed sample. A region near the tip of the sheaf in (a) is enlarged in (b). The arrows in (b) indicate possible sub-operational embryos which are much smaller than the fully grown sub-units seen in (a). After Olson *et al*. (1989).

140

and expressed their results empirically as:

$$B_S{}^\circ C = 830 - 270w_C - 90w_{Mn} - 37w_{Ni} - 70w_{Cr} - 83w_{Mo} \tag{6.14}$$

where w_i is the wt% of element i in solid solution in austenite.

6.5 The Nucleation Rate

The linear dependence of the activation energy for nucleation on the driving force can be substituted into a nucleation rate equation to obtain:[†]

$$
\begin{aligned}
I_V &= C_3 \exp\left\{ -\frac{G^*}{RT} \right\} \\
&= C_3 \exp\left\{ -\frac{C_4 + C_5 \Delta G_m}{RT} \right\}
\end{aligned}
\tag{6.15}
$$

where ΔG_m is the maximum value of ΔG_{CHEM} (Fig. 6.2c) and C_i are positive constants. The nucleation rate at T_h is obtained by setting $\Delta G_m = G_N$

$$I_{T_h} = C_3 \exp\left\{ -\frac{C_4 + C_5 G_N}{RT_h} \right\} \tag{6.16}$$

It follows that

$$I_V = I_{T_h} \exp\left\{ -\frac{C_4 \Delta T}{RTT_h} - \frac{C_5}{R}\left(\frac{\Delta G_m}{T} - \frac{G_N}{T_h} \right) \right\} \tag{6.17}$$

with $\Delta T = T_h - T$. Recall that the G_N function was justified with martensite nucleation theory assuming that the nucleation rate I_{T_h} is the same for all steels at T_h. For two different steels A and B,

$$\frac{I_{T_h^A}}{I_{T_h^B}} = \exp\left\{ -\frac{(C_4 - C_2 C_5)(T_h^A - T_h^B)}{RT_h^A T_h^B} \right\} \tag{6.18}$$

Since $I_{T_h^A} = I_{T_h^B}$ it follows that $C_4 = C_2 \times C_5$ so that

$$I_V = C_3 \exp\left\{ -\frac{C_4}{RT} - \frac{C_4 \Delta G_m}{C_2 RT} \right\} \tag{6.19}$$

In this equation the constant C_2 is known since it comes from the slope of the G_N function (equation 6.1) so the two unknowns are C_3 and C_4 which are obtained by fitting to experimental data. The pre-exponential factor C_3 is the product of a number density of nucleation sites (N_V^0) and an attempt frequency (ν).

[†]Bhadeshia (1982b); Rees & Bhadeshia (1992); Chester & Bhadeshia (1997); Singh (1998).

6.6 Growth Rate

The displacement of an interface requires the atoms of the parent to transfer into and adopt the crystal structure of the product phase. The ease with which this happens determines the interface mobility. There may also be a partitioning of solutes in which case diffusion may limit the movement of the interface. The two processes of diffusion and mobility are in series; the velocity as calculated from the interface mobility must therefore match that due to the diffusion of solute ahead of the interface. Both processes dissipate the available free energy, so motion is always under mixed control. However, a process is said to be diffusion-controlled when most of the free energy is dissipated in the diffusion of solute. Interface-controlled growth occurs when the larger proportion of the free energy is consumed in the transfer of atoms across the interface. The compositions of the phases at the moving interface during diffusion-controlled growth are given approximately by a tie-line of the phase diagram, and other circumstances are illustrated in Fig. 6.11.
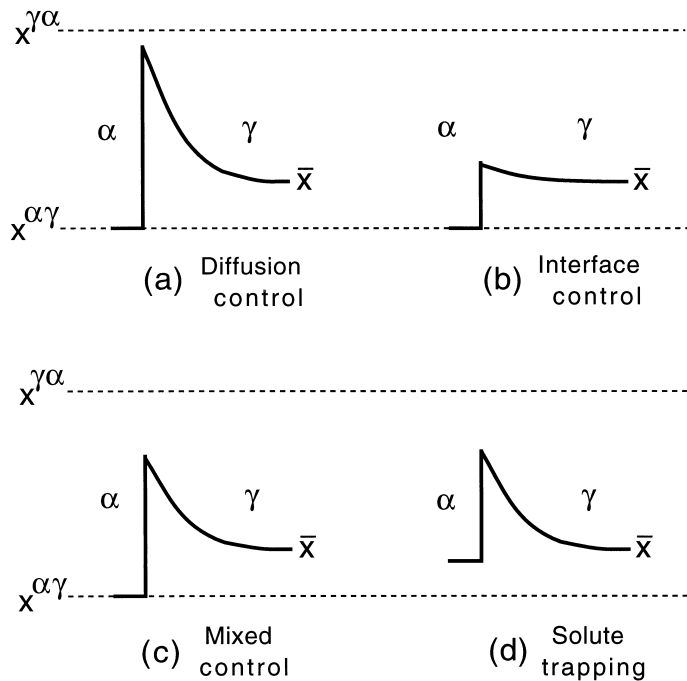

Fig. 6.11 Carbon concentration profiles at a moving α/γ interface. The terms $x^{\alpha\gamma}$, $x^{\gamma\alpha}$ and $\bar{x}$ refer to the equilibrium concentrations in the ferrite and austenite respectively, and the average concentration in the alloy as a whole. (a) Diffusion control. (b) Interface control. (c) Mixed control. (d) Solute trapping (discussed later).

142

6.6.1 Theory for the Lengthening of Plates

Particle dimensions during diffusion-controlled growth vary parabolically with time when the extent of the diffusion field increases with particle size. The growth rate thus decreases because the solute has to diffuse over ever increasing distances to reach the far-field concentration. Plates or needles can however grow at a constant rate because solute can be partitioned to their sides.

The partitioning of interstitial elements during displacive transformation should lead to diffusion-controlled growth because the glissile interface necessary for such transformation has the highest mobility. Iron and any substitutional solute atoms do not diffuse so their role is purely thermodynamic.

Trivedi (1970) has solved for the diffusion-controlled growth of plates whose shape approximates that of a parabolic cylinder (Fig. 6.12). The plate lengthening rate V_l at a temperature T for steady state growth is obtained by solving:

$$f_1 = \frac{x_r - \overline{x}}{x_r - x^{\alpha\gamma}}$$

$$f_1 = (\pi p)^{0.5} \exp\{p\} \mathrm{erfc}\{p^{0.5}\} \left[1 + \frac{V_l}{V_c} f_1 S_1\{p\} + \frac{r_c}{r} f_1 S_2\{p\} \right] \qquad (6.20)$$

where the Péclet number is
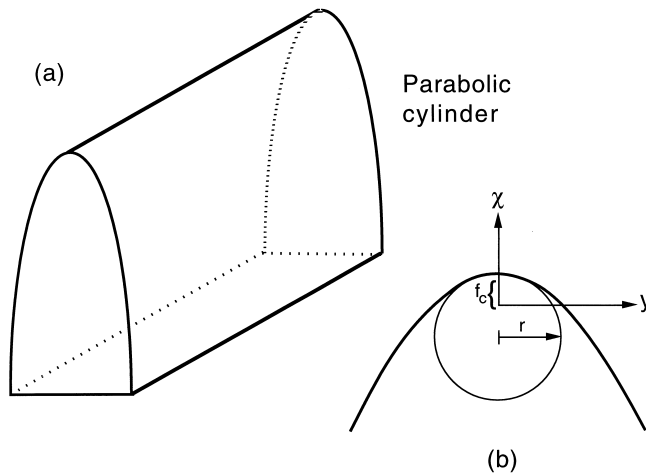
$$p = V_l r / 2\overline{D} \qquad (6.21)$$

Fig. 6.12 (a) An illustration of the shape of a parabolic cylinder. (b) Definitions of the tip radius r, the focal distance f_c and the coordinates.

143

The weighted-average diffusion coefficient $\overline{D}$ for carbon in austenite is given by integrating D (the diffusivity at a specific concentration) over the range $\overline{x}$ to x_r, and then dividing the integral by this range.

The function $S_2\{p\}$ of equation 6.21 depends on the Péclet number (Fig. 6.13); it corrects for variation in composition due to changing curvature along the interface and has been evaluated numerically by Trivedi. The term containing S_1 is prominent when growth is not diffusion-controlled; V_c is the interface-controlled growth velocity of a flat interface. For diffusion-controlled growth, which is discussed first, V_c is very large when compared with V_l and the term containing it can be neglected.

x_r is the carbon concentration in the austenite at the plate tip. It may differ from the equilibrium carbon concentration $x^{\gamma\alpha}$ because of the Gibbs–Thompson capillarity effect (Christian, 1975); x_r decreases as interface curvature increases, and growth ceases at a critical radius r_c when $x_r = \overline{x}$. For a finite plate tip radius,

$$x_r = x^{\gamma\alpha}[1 + (\Gamma/r)] \tag{6.22}$$

where Γ is the capillarity constant given by (Christian, 1975):

$$\Gamma = \frac{\sigma^{\alpha\gamma} V_m}{RT} \frac{(1 - x^{\gamma\alpha})}{(x^{\alpha\gamma} - x^{\gamma\alpha})} \left[1 + \frac{d(\ln f_C\{x^{\gamma\alpha}\})}{d(\ln x^{\gamma\alpha})}\right]^{-1} \tag{6.23}$$

where $\sigma^{\alpha\gamma}$ is the interfacial energy per unit area, f_C is the activity coefficient of carbon in austenite, and V_m is the molar volume of ferrite. This assumes that the ferrite composition is unaffected by capillarity, since $x^{\alpha\gamma}$ is always very small. The critical plate tip radius r_c can be obtained by setting $x_r = \overline{x}$.
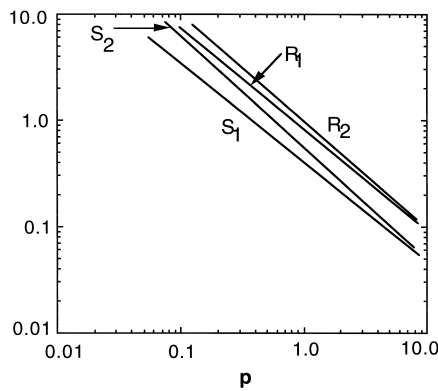

Fig. 6.13 Dependence of Trivedi's functions S_1, S_2, R_1 and R_2 on the Péclet number p.

Trivedi's solution for diffusion-controlled growth assumes a constant shape, but the solution is not strictly shape-preserving. The concentration x_r varies over the surface of the parabolic cylinder which should lead to a deviation from the parabolic shape. Trivedi claims that the variation in x_r has a negligible effect provided the tip radius is greater than $3r_c$.

Plate growth theory provides a relation between velocity and tip radius (Fig. 6.14). Additional theory is required to enable the choice of a particular tip radius and hence to fix V_l. Small tip radii favour fast growth due to the point effect of diffusion, but this is counteracted by the capillarity effect. Zener proposed that the plate should tend to adopt a tip radius which allows V_l to be maximised but this remains a hypothesis. Work on the dendritic growth of solid from liquid (formally an almost identical problem) has shown that the dendrites do not select the radius corresponding to the maximum velocity. The radius is determined instead by a shape stability criterion (Glicksman *et al.*, 1976; Langer and Muller-Krumbhaar, 1978). If these results can be extrapolated to displacive transformations, and it is doubtful that they can given that the shape is constrained by strain energy minimisation, then calculated velocities would be greatly reduced. This does not fit experimental data where the lengthening rate is slightly higher that the maximum velocity predicted theoretically (Bhadeshia, 1985a).

The shape of ferrite plates is sometimes more needle-like (lath) than plate-like. Trivedi has obtained a steady-state solution for the diffusion-controlled growth of paraboloids of revolution (i.e. needles):

$$f_1 = p \exp\{p\} \text{Ei}\{p\} \left[1 + \frac{V_l}{V_c} f_1 R_1\{p\} + \frac{r_c}{r} f_1 R_2\{p\} \right] \qquad (6.24)$$

The tip radius r_c is twice as large as that for plates because there are two radii of curvature for a needle tip.
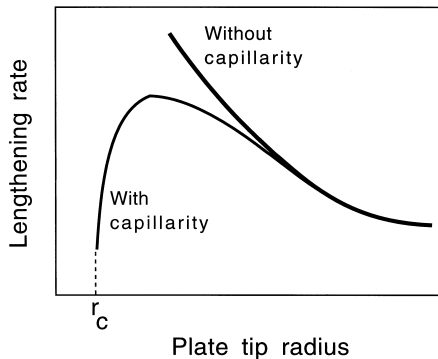

Fig. 6.14 Variation in lengthening rate as a function of the plate tip radius.

6.6.2 Growth Rate of Sheaves of Bainite

After nucleating at austenite grain surfaces, sheaves of bainite propagate by the repeated formation of sub-units, each of which grows to a limited size. New sub-units are favoured near the tips of existing platelets; nucleation in adjacent positions occurs at a much lower rate. Therefore, the overall shape of the sheaf is also that of a plate in three dimensions with growth limited only by austenite grain or twin boundaries.

Most direct observations have used optical microscopy and hence monitor the growth of *sheaves* rather than of the transformation unit which is only about 0.2 μm in thickness. Suppose that a sub-unit reaches its limiting size in a time period t_C, and that a time interval Δt elapses before the next one is stimulated, then the lengthening rate, V_S, of a sheaf is given by:

$$V_S = V_l \left(\frac{t_C}{t_C + \Delta t} \right) \tag{6.25}$$

where V_l is the average lengthening rate of a sub-unit.

Bainite sheaves lengthen at a constant rate although the data show considerable scatter, attributed to stereological effects (Speich and Cohen, 1960; Goodenow *et al.*, 1963; Hawkins and Barford, 1972). Greater concentrations of carbon, nickel or chromium concentration reduce V_S. The growth of sheaves seems to occur at a constant aspect ratio although thickening continues when lengthening has stopped. This is not surprising since the sheaf can continue to grow by the sub-unit mechanism until the T_0' condition is achieved.

An assessment of sheaf data shows that the lengthening rate is greater than expected from diffusion-controlled growth, Fig. 6.15. This includes measurements on Fe–Ni–C alloys which are frequently (incorrectly) used to justify the existence of some sort of a solute drag effect.

6.6.3 Growth Rate of Sub-Units of Bainite

The growth rate of martensite can be so fast as to be limited only by the speed of sound in the metal. Although bainite grows rapidly, the lengthening rate is much smaller than that for martensite. The interface moves relatively slowly even though it is glissile. This is probably because of the plastic work that is done as the bainite grows. A good analogy is to compare brittle failure in a glass where cracks propagate rapidly, with cleavage failure in metals which is not as rapid because of the plastic zone which has to move with the crack tip.

The lengthening rate of sub-units has been measured using hot-stage photo-emission electron microscopy. Electrons are excited from the surface of the sample using incident ultraviolet radiation, and it is these photo-emitted electrons which form the image. The technique can resolve individual sub-units of
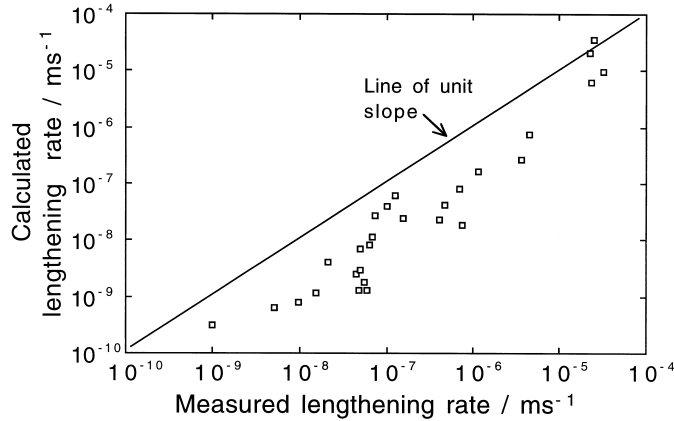
Fig. 6.15 Comparison of published data on the lengthening rate of bainite sheaves against those calculated assuming paraequilibrium carbon-diffusion controlled lengthening (Ali and Bhadeshia, 1989).

bainite. Fig. 6.16 illustrates a series of photoemission electron micrographs taken at 1 s intervals, showing the growth of bainite sub-units. The measured lengthening rate of the arrowed sub-unit is $75\,\mu\text{m s}^{-1}$. This is many orders of magnitude larger than calculated assuming paraequilibrium at the transformation front $(0.083\,\mu\text{m s}^{-1})$. Lengthening occurs at a rate much faster than expected from carbon diffusion-control growth.

There are interesting observations on the thickening of bainite sub-units. The thickness can increase even after lengthening has halted. An elastically accommodated plate tends to adopt the largest aspect ratio consistent with a balance between the strain energy and the free energy change driving the transformation, Fig. 6.17, in order to achieve thermoelastic equilibrium (Olson and Cohen, 1977).

Bainite plates are not elastically accommodated but it should be possible for the thickness of a plate to increase at constant length if the process is captured at an early stage. Fig. 6.17b shows a large plate of bainite which formed first followed by smaller orthogonal plates. The larger plate is seen to bow between the smaller plates whose tips act as pinning points. The smoothly curved regions of the interface between the pinning points prove that the interface moves continuously rather than by a step mechanism.

6.6.4 Solute Drag

Solute drag is a process in which free energy is dissipated in the diffusion of solute atoms *within the interface*; these are the atoms which in a stationary
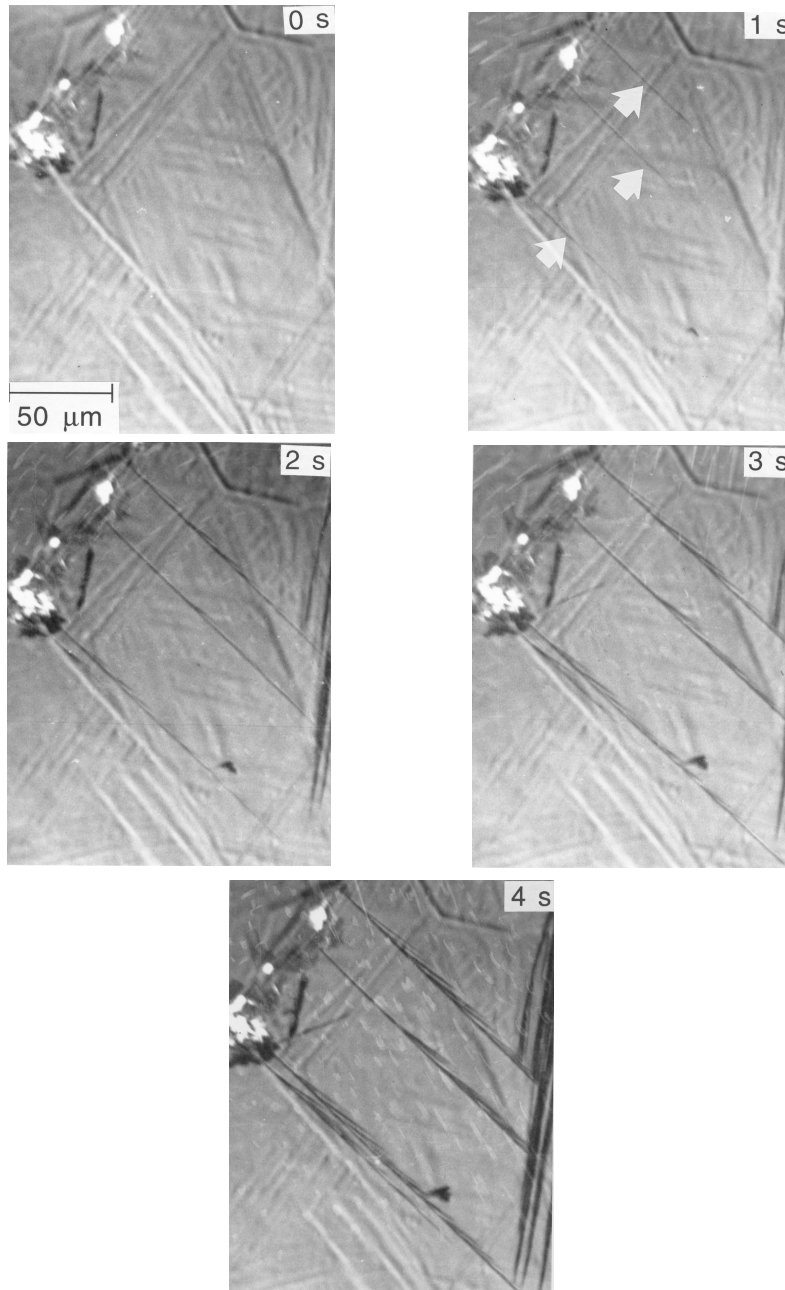
Fig. 6.16 Photoemission electron microscope observations on the growth of individual sub-units in a bainite sheaf (Bhadeshia, 1984). The pictures are taken at 1 s intervals during transformation at 380 °C in a Fe–0.43C–2.02Si–3Mn wt% alloy. The micrograph at 0 s is fully austenitic, the relief being a residue from an earlier experiment.
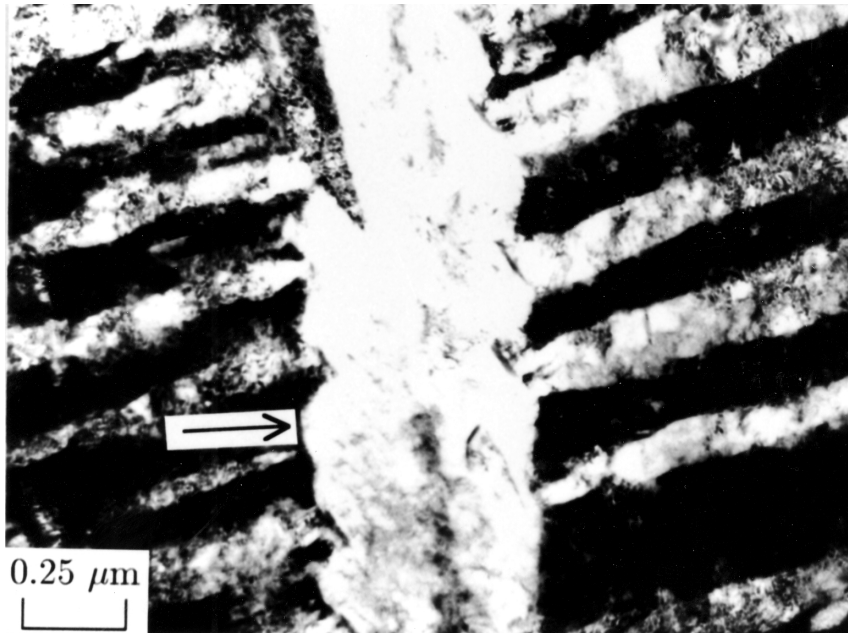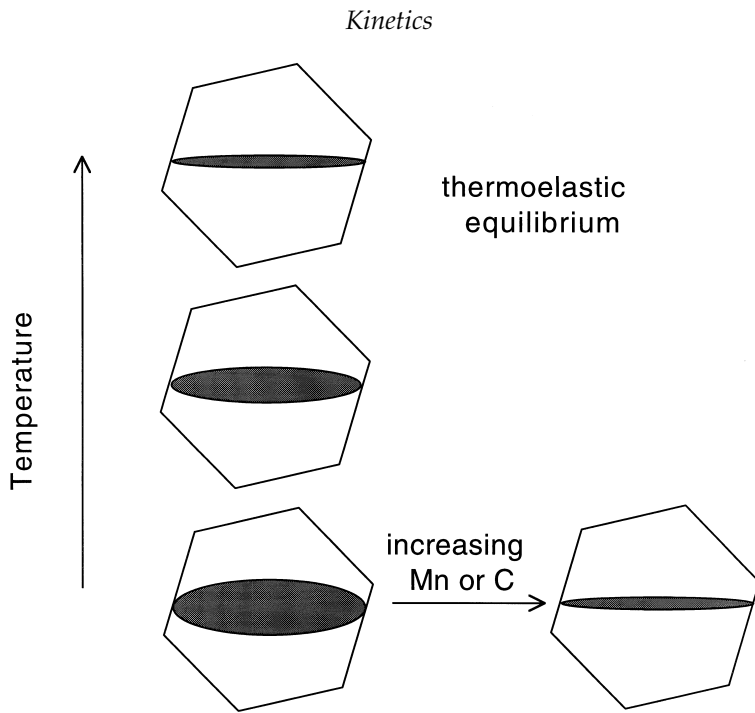
148

Fig. 6.17 (a) Effect of thermoelastic equilibrium on the aspect ratio of a plate with a fixed length. (b) Bowing of α_b/γ interface at strong pinning points, particularly prominent in regions identified by arrows (Chang and Bhadeshia, 1995b).

149

interface are said to be segregated or desegregated in the structure of the interface. The phenomenon is similar to the drag on dislocations when atoms are attracted to the dislocation cores. Chapter 2 contains a discussion of the atomic resolution experiments which show that there is no excess concentration of solute at the bainite/austenite interface. Consequently, there is no reason to expect solute drag effects during the bainite reaction.

6.7 Partitioning of Carbon from Supersaturated Bainitic Ferrite

It is better for the carbon that is trapped in bainite to partition into the residual austenite where it has a lower chemical potential. Consider a plate of thickness w with a one-dimensional flux of carbon along z which is normal to the α/γ interface, with origin at the interface and z defined as positive in the austenite (Kinsman and Aaronson, 1967). A mass conservation condition gives (Bhadeshia, 1988):

$$\frac{1}{2}w(\overline{x} - x^{\alpha\gamma}) = \int_0^\infty [x_\gamma\{z, t_d\} - \overline{x}]dz \tag{6.26}$$

where $x^{\alpha\gamma}$ and $x^{\gamma\alpha}$ are the paraequilibrium carbon concentrations in α and γ respectively, allowing for stored energy. Since the diffusion rate of carbon in austenite is slower than in ferrite, the rate of decarburisation will be determined by the diffusivity in the austenite. The concentration of carbon in austenite at the interface remains constant for times $0 < t < t_d$, after which it steadily decreases as homogenisation occurs. The concentration profile in the austenite is given by:

$$x_\gamma = \overline{x} + (x^{\gamma\alpha} - \overline{x})\text{erfc}\left\{\frac{w}{2(\overline{D}t_d)^{\frac{1}{2}}}\right\} \tag{6.27}$$

which on integration gives:

$$t_d^{\frac{1}{2}} = \frac{w(\overline{x} - x^{\alpha\gamma})\pi^{\frac{1}{2}}}{4\overline{D}^{\frac{1}{2}}(x^{\gamma\alpha} - \overline{x})} \tag{6.28}$$

Some results from this analysis are illustrated in Fig. 6.18.

Equation 6.28 does not allow for the coupling of fluxes in the austenite and ferrite. It assumes that the diffusivity in the ferrite is so large, that any gradients there are eliminated rapidly. A flux balance must in general be satisfied as follows:

$$D_\alpha \frac{\partial x^\alpha}{\partial z} = \overline{D}\frac{\partial x^{\gamma\alpha}}{\partial z} \tag{6.29}$$

where D_α is the diffusivity of carbon in the ferrite, x^α is the concentration of carbon in the ferrite at the interface with the gradients evaluated at the interface. Since $D_\alpha \gg D_\gamma$, x^α will inevitably deviate from $x^{\alpha\gamma}$ in order to maintain the flux balance. It will only reach the equilibrium value towards the end of the partitioning process. The gradients in the ferrite must also increase with $x^{\gamma\alpha}$; the partitioning process could then become limited by diffusion in the ferrite. As a consequence, the diffusion time as predicted by the finite difference method becomes larger than that estimated by the approximate analytical equation when the transformation temperature is decreased or $x^{\gamma\alpha}$ increased, as illustrated in Fig. 6.18. Typical concentration profiles that develop during the partitioning process are illustrated in Fig. 6.19.

The assumption throughout that during the decarburisation process $x^{\gamma\alpha}$ is fixed at the value given by paraequilibrium between ferrite and austenite is hard to justify since $x^\alpha \neq x^{\alpha\gamma}$. Hillert *et al.* (1993) have avoided this assumption; it is interesting that the results they obtain are not essentially different from those presented above.
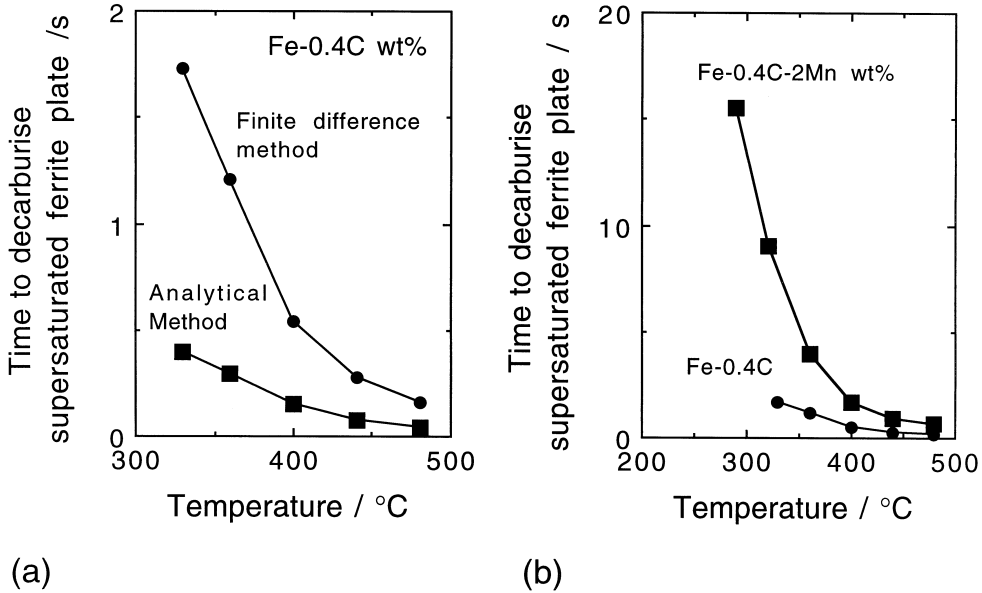

(a) (b)

Fig. 6.18 (a) The time to decarburise a plate of thickness 0.2 μm. Calculations using the analytical and finite difference methods are illustrated. (b) The effect of adding an austenite stabilising substitutional solute on the decarburisation time (Mujahid and Bhadeshia, 1992).
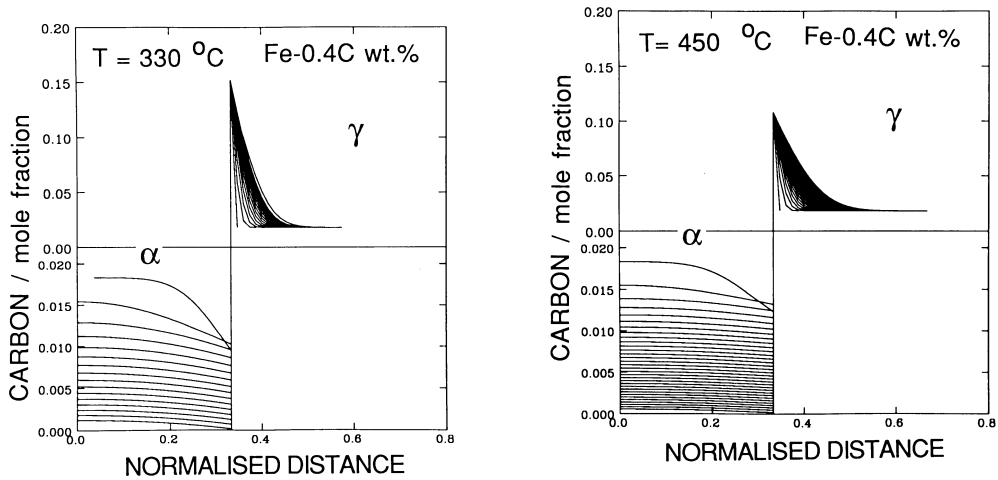
151

Fig. 6.19 The concentration profiles that develop in ferrite and and austenite during the partitioning of carbon from supersaturated bainite (Fe–0.4C wt%, plate thickness 0.2 μm). (a) 330 °C, the time interval between the concentration contours in each phase being 0.094 s. (b) 450 °C, the corresponding time interval is 0.007 s. (Mujahid and Bhadeshia, 1992).

6.8   Growth with Partial Supersaturation

(i) A transformation can occur without any composition change as long as there is a reduction in the free energy. The chemical potential is then nonuniform across phase boundaries for all of the atomic species. A net reduction in free energy is still possible because some of the species are trapped in the parent phase and others in the product. Thus, martensitic transformation of steel involves the trapping of carbon in the martensite and iron in the austenite.

(ii) Equilibrium transformation requires the partitioning of solutes between the phases until the chemical potential for each species is uniform in all locations.

(iii) In paraequilibrium only carbon has a uniform chemical potential - the substitutional and iron atoms are trapped in the parent or product phases.

These three cases of composition-invariant, equilibrium and paraequilibrium transformation are well-defined. We now deal with the case where the extent of carbon partitioning is between paraequilibrium and composition-invariant transformation:

$$x^{\alpha\gamma} \leq x^{\alpha} \leq \overline{x} \qquad \text{and} \qquad \overline{x} \leq x^{\gamma} \leq x^{\gamma\alpha}$$

152

Some of the carbon is trapped in the product phase but a proportion partitions so that the differences in chemical potential are reduced. The ferrite grows with a *partial supersaturation*, the level of which is fixed by kinetic constraints which we shall now consider.

6.8.1 Stability

In Fig. 6.20, x_m represents the maximum concentration of carbon that can be tolerated in ferrite which precipitates from austenite of composition $\overline{x}$. A higher concentration cannot be sustained because there would be an increase in free energy on transformation.

Growth with partial supersaturation, such as the case where the interface compositions are given by $x^\alpha = x_m$ and $x^\gamma = \overline{x}$ is expected to be unstable to perturbations since the concentration field must tend to adjust towards lower free energy states. The assembly should then irreversibly cascade towards the equilibrium partitioning of carbon with $x^\alpha = x^{\alpha\gamma}, x^\gamma = x^{\gamma\alpha}$. Experimental evidence supports this conclusion since the growth rate of Widmanstätten ferrite is found to be consistent with the paraequilibrium partitioning of carbon at all transformation temperatures. These considerations do not necessarily rule out the possibility of carbon trapping because some other physical phenomenon could provide the necessary stabilising influence (Christian and Edmonds, 1984).

There are many processes, including diffusion, which occur in series as the ferrite grows. Each of these dissipates a proportion of the free energy available for transformation. For a given process, the variation in interface velocity with dissipation defines a function which in recent years has been called an *interface*
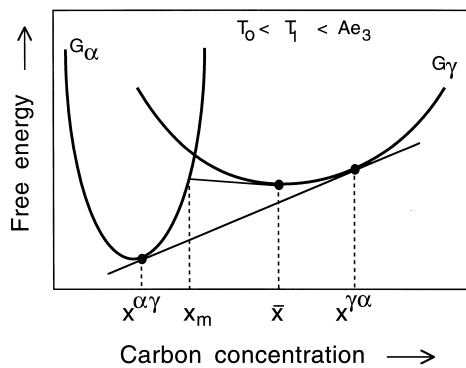

Fig. 6.20 Austenite and ferrite free energy curves illustrating the unstable nature of an assembly in which the ferrite forms with a partial supersaturation of carbon.

response function. The actual velocity of the interface depends on the simultaneous solution of all the interface response functions, a procedure which fixes the composition of the growing particle.

Figure 6.21 shows an electrical analogy; the resistors in series are the hurdles to the movement of the interface. They include diffusion in the parent phase, the transfer of atoms across the interface, solute drag, etc. The electrical-potential drop across each resistor corresponds to the free energy dissipated in each process, and the current, which is the same through each resistor, represents the interface velocity. The relationship between the current and potential is different for each resistor, but the actual current is obtained by a simultaneous solution of all such relations.

Following on from this analogy, the available free energy can be partitioned into that dissipated in the diffusion of carbon, a quantity expended in the transfer of atoms across the interface, and in any other process determining the motion of the interface. There are three unknowns: the austenite composi-
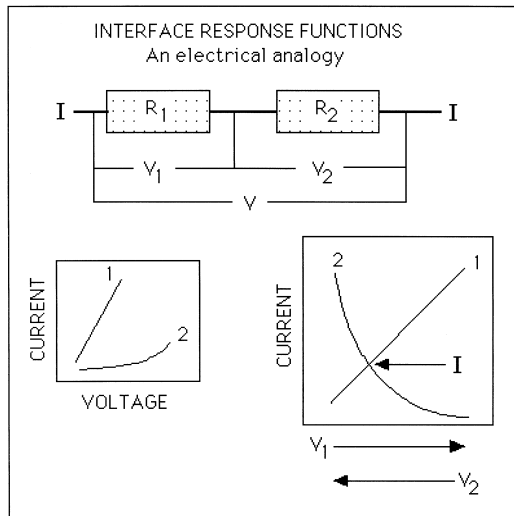

Fig. 6.21 An electrical analogy illustrating the dissipations due to processes which occur in series as the transformation interface moves. The resistors in series are the hurdles to the motion of the interface, the voltage the driving force and the current the interface velocity. The way in which voltage (driving force) is dissipated as a function of current (velocity) across each resistor is different, since each resistor represents a separate physical process. There is only one interface so all these processes must yield the same velocity, as indicated by the identical current passing through all the resistors.

154

tion at the interface, the supersaturation and the velocity, so it is necessary to exploit at least three interface response functions. If the tip radius of the plate is considered to be a variable, then the number of unknowns is four; for displacive transformations the radius can be assumed to be fixed by strain energy minimisation. The necessary three interface velocity functions are, therefore, the diffusion field velocity, the velocity determined from interface mobility and a carbon trapping function. Each of these is now discussed in detail.

But to summarise first, the response functions all give different velocities for a given free energy dissipation. The total driving force has to be partitioned into the individual dissipations in such a way that all the response functions give an identical velocity.

6.8.2 The Interface Response Functions

6.8.2.1 The Interface Mobility (Martensitic Interface)

The interfacial mobility is formulated using the theory for thermally activated motion of dislocations (Olson *et al.*, 1989, 1990). This is justified because a glissile interface consists of an array of appropriate dislocations. The interfacial velocity V_i is then given by:

$$V_i = V_o \exp \left\{ -\frac{G*}{kT} \right\} \tag{6.30}$$

where G^* is an activation free energy and the pre-exponential factor V_o can be taken to be $30\,\mathrm{m\,s^{-1}}$ based on experimental data from single-interface martensitic transformations (Grujicic *et al.*, 1985). The activation energy G^* is a function of the net interfacial driving force G_{id} through the relation (Kocks *et al.*, 1975):

$$G^* = \int_{G_{id}}^{G'_{id}} v^* dG \tag{6.31}$$

where G'_{id} is the maximum resistance to the glide of interfacial dislocations and v^* is the activation volume swept by the interface during a thermally activated event. For a wide range of obstacle interactions, the function $G^*\{G_{id}\}$ can be represented by:

$$G^* = G_o^* \left[1 - \left(\frac{G_{id}}{G'_{id}} \right)^y \right]^z \tag{6.32}$$

where G_o^* is the activation free energy barrier to dislocation motion in the absence of an interfacial driving force. The constants y and z define the shape of the force-distance function and for solid-solution interactions in the

155

Labusch limit (where hardening is due to the average effect of many strain centres), it may be assumed that $y = 0.5$ and $z = 1$ (Nabarro, 1982).[†]

Analysis of kinetic data for the interface-controlled nucleation of martensite gives

$$G_o^* = 0.31 \mu \Omega \qquad (6.33)$$

where μ is the shear modulus of the matrix and Ω is the volume per atom. Based on the behaviour of Fe–Ni–C alloys (Olson, 1984), G_{id}' is taken to be:

$$G_{id}' = 1.22 \times 10^{-3} \mu \qquad (6.34)$$

6.8.2.2 The Interface Mobility Based on Absolute Reaction Rate Theory

An empirical model is sometimes used to represent the interface mobility for displacive transformations (Hillert, 1960; Ågren, 1989). It uses chemical rate theory, one of the assumptions of which is that the 'reaction' consists of the repetition of unit steps involving the interaction of a small number of atoms. Whereas this may be justified for a process like solidification, the assumptions of chemical rate theory are unlikely to be applicable to displacive transformations in which a large number of atoms move in a disciplined manner.

The interface velocity is given by (Christian, 1975):

$$V_i = \delta_b f^* \exp\left\{ -\frac{G^*}{RT} \right\} \left[1 - \exp\left\{ -\frac{G_{id}}{RT} \right\} \right] \qquad (6.35)$$

where δ_b is the thickness of the interface, and f^* is an attempt frequency for atomic jumps across the interface. For small G_{id} the equation simplifies to

$$V_i = M G_{id} \qquad (6.36)$$

where M is a mobility, estimated by Hillert (1975) for reconstructive transformations to be:

$$M = 0.035 \exp\left\{ -\frac{17700}{T} \right\} \qquad m^4\,J^{-1}\,s^{-1} \qquad (6.37)$$

6.8.2.3 The Diffusion Field Velocity

The diffusion field velocity depends on the compositions of the phases at the interface. These compositions are illustrated in Fig. 6.22, on a free energy diagram as a function of the amount G_{dd} of free energy dissipated in the diffusion

[†]The relationship between the activation energy and driving force is here nonlinear, compared with equation 6.10 of the nucleation theory. The nonlinear function is a better approximation but the linear relation of equation 6.10 suffices for most purposes.
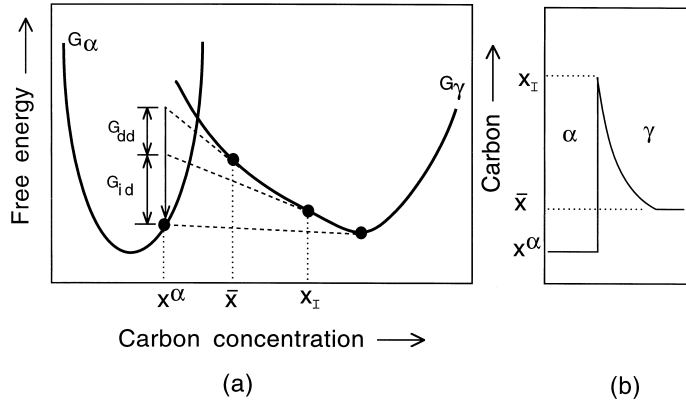
Fig. 6.22 (a) Constant temperature free-energy curves showing the quantities G_{dd} and G_{id} for the case where the interface compositions are as illustrated in (b). Note that the net free energy available for interfacial motion *after* allowing for strain energy and interface energy contributions is ΔG, which is the sum of the two dissipations G_{dd} and G_{id}.

of solute ahead of the interface. The concentrations x^α and x_I are not independent because the choice of either fixes the value of the other uniquely.

The Trivedi solution for plates is probably the best available for diffusion-controlled growth, but there are more convenient approximations. One of these is due to Ivantsov (1947), in which the growth of a parabolic cylinder shaped particle is treated without the inclusion of interface mobility and capillarity effects. The velocity V_d for steady state growth of ferrite of constant composition x^α in a steel of composition $\overline{x}$ is given by:

$$\frac{\overline{x} - x_I}{x^\alpha - x_I} = (\pi p)^{\frac{1}{2}} \exp\{p\} \mathrm{erfc}\{p^{\frac{1}{2}}\} \tag{6.38}$$

where x_I is the carbon concentration in the austenite at the interface and p is the Péclet number.

6.8.2.4 Solute Trapping Law

Atoms are forced into the product phase during martensitic transformation. The chemical potential of some of these atoms increases as they are engulfed by the martensite. Similarly, during paraequilibrium transformation some of the immobile substitutional-solutes are forced into the growing crystal. A solute or solvent is said to be trapped when its chemical potential increases on transfer across the interface. The term *solute trapping* is relatively recent (Baker and Cahn, 1969, 1971) but the phenomenon has been known for much longer in the context of transformations in steels.

157

Figure 6.23 illustrates a transformation front between the shaded and unshaded crystals, in a binary alloy containing *A* (solvent) and *B* (solute) atoms. The smaller solute atoms prefer to be in the parent phase (γ). The atoms in the central layer have to move along the vectors indicated in order to transform into the product phase (α). λ is a typical diffusion jump distance for the solute atom; the motions required for the atoms in the interfacial layer to adjust to the new crystal structure are rather smaller.

Solute will be trapped if the interface velocity V_k is greater than that at which solute atoms can diffuse away. The maximum diffusion velocity is approximately D/λ since λ is the minimum diffusion distance, so that trapping occurs when $V_k > D/\delta_s$.

The Aziz model (1982, 1983) relates interfacial velocity to the partitioning coefficient k_p, which is the ratio of the concentration in the product phase at the interface to that in the parent phase at the interface:

$$k_p = x^\alpha / x_I \tag{6.39}$$

and $k_p = k_e$ where k_e is the equilibrium partition coefficient.

There are two basic mechanisms of interface displacement, one involving propagation by the displacement of steps, and the other by the displacement of
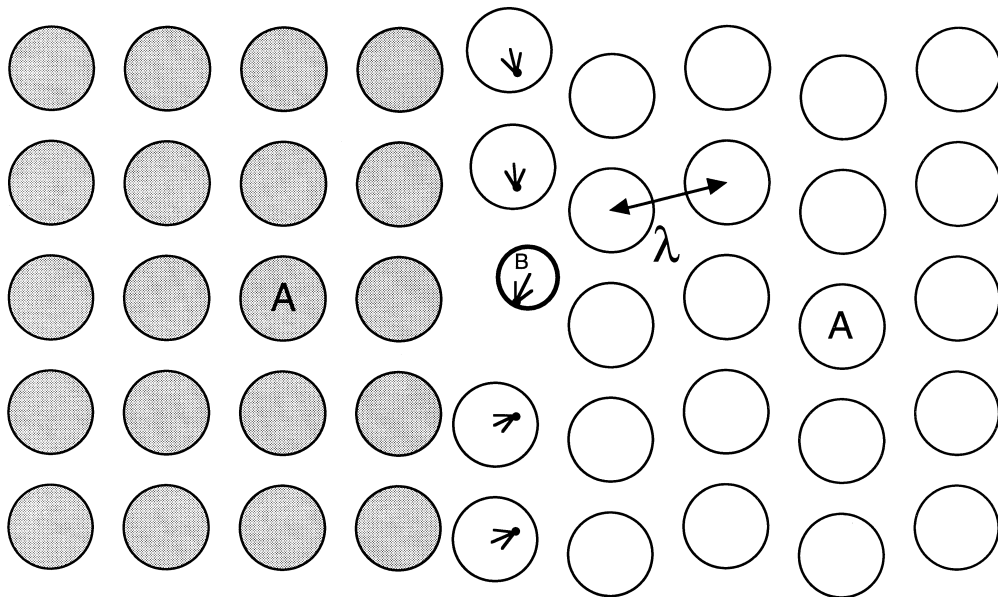

Fig. 6.23 Choreography of solute trapping, adapted from Aziz (1982). The solvent is labelled *A*, solute *B* and the product phase is shaded dark. The transformation front is advancing towards the right.

158

all elements of the boundary; this latter mechanism is called 'continuous' motion. Aziz has derived slightly different trapping models for these two cases. The step model only permits transformation below the T_0' temperature of the austenite in the vicinity of the interface. This is in general too restrictive and certainly inapplicable for transformations at temperatures above the T_0' temperature, of the type being considered here. Goldman and Aziz (1987) have proposed another model for stepped growth, which they call the *aperiodic step model*, in which the steps are assumed to pass at random intervals with transformation restricted to below the T_0' temperature of the parent phase at the interface. The trapping law turns out to be the same as for the continuous growth model which is suitable for transformation above T_0'.

The trapping model gives a velocity function of the form

$$V_k = \frac{D\{x_I\}}{\lambda} \frac{k_p - k_e}{1 - k_p} \tag{6.40}$$

where λ, the intersite jump distance is about 0.25 nm and $D\{x_I\}$ is the diffusion coefficient of carbon in austenite of composition x_I. The quantity $D\{x_I\}/\lambda$ is the diffusion velocity of carbon and trapping becomes prominent when the interface velocity approaches this value. Since the carbon atoms execute jumps across a glissile semi-coherent interface it is appropriate to take the coefficient for volume diffusion of carbon.

We now have the third interface response function (equation 6.40) which varies smoothly with x^α and x_I. Note that as x^α approaches $\bar{x}$, the diffusion field velocity diverges (tends towards infinity) and the interfacial dissipation then imposes the condition that $x_I = \bar{x}$ such that the trapping velocity V_k also tends towards infinity in the full trapping limit.

6.8.3 Calculated Data on Transformation with Partial Supersaturation

We now consider results from the two main models for growth involving a partial supersaturation of carbon, that due to Olson *et al.* (1987, 1989, 1990) and, due to Hillert (1960, 1975) and Ågren (1989).

With the three interface response functions, the diffusion field velocity (Ivantsov model, with a plate-tip radius fixed at 1.5 nm), the glissile-interface mobility function and the Aziz solute trapping function, Olson *et al.* solved for the interfacial velocity and phase compositions as a function of transformation temperature. Some of their results are presented in Fig. 6.24a, for a Fe–0.4C wt% alloy, illustrating how the supersaturation might vary with the transformation temperature for both the nucleation and growth stages. With a variety of assumptions about the strain energy of transformation and about the
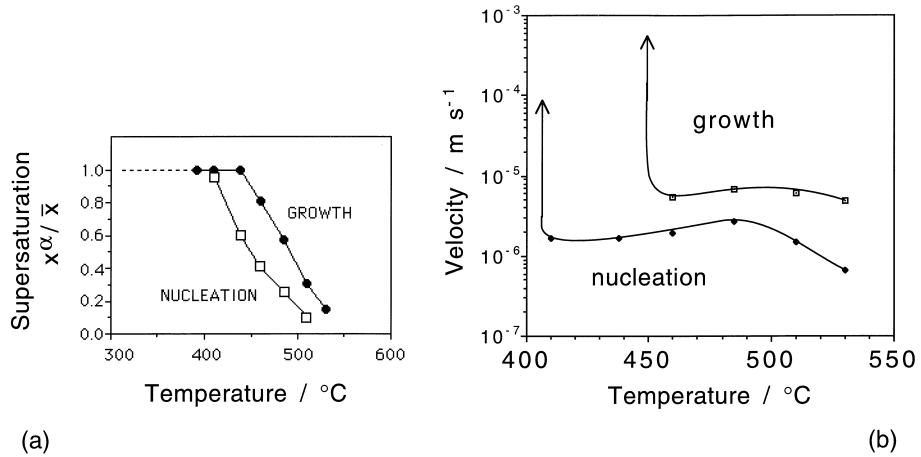
159

Fig. 6.24 (a) Plot of calculated normalised supersaturation $(x^{\alpha}/\overline{x})$ of carbon in ferrite versus the isothermal transformation temperature, for a Fe–0.4C wt% alloy, with the data obtained by the simultaneous solution of the interfacial mobility, diffusion field velocity and trapping velocity functions. Martensitic transformation is when both nucleation and growth become diffusionless. (b) The interfacial velocities during the 'nucleation' and growth processes.

nucleation behaviour, the model has been shown to compare favourably with the measured TTT diagram.

The calculations have been extended to cover a wider range of carbon concentrations. Malecki (1990) found that for high carbon steels the model is not able to predict the acceleration of the bainite reaction at temperatures just above M_S, first noted by Howard and Cohen (1948) and discussed later in this Chapter. Mujahid and Bhadeshia (1993) found that the M_S temperature is predicted accurately if it is assumed that both nucleation and growth are diffusionless for martensite. The variation in the B_S temperature as a function of the carbon concentration could also be estimated. However, the absolute values of B_S could only be brought into agreement with experimental data by allowing the stored energy to be a function of temperature.

The model by Hillert and Ågren is founded on the theory for reconstructive transformations. The interface mobility function used relies on absolute reaction rate theory, which is not appropriate for glissile interfaces. The radius of curvature at the plate tip is treated as a free variable. It is assumed that the curvature adopted is that which gives the highest growth rate. Strain energy due to the mechanism of transformation is neglected. To solve for the three unknowns (austenite and ferrite compositions and the interfacial velocity), a

160

solute drag function due to Hillert and Sundman (1976) is utilised in addition to the interface mobility and diffusion field velocity response functions. It is predicted that there is a gradual transition from diffusion-controlled to diffusionless growth as the driving force is increased, although the plate shape is then lost because diffusionless growth occurs with zero interface curvature, i.e. a flat interface!

6.8.4 Summary

Both of the models predict an increase in carbon trapping as the transformation temperature is reduced. They establish the possibility that the transition from bainite to martensite is gradual. However, there remain numerous difficulties.

An increasing supersaturation with undercooling is inconsistent with the fact that the bainite reaction stops when the carbon concentration of the residual austenite approaches the T_0' curve. According to the calculations the carbon concentration of the austenite when transformation stops should be that given by the Ae_3'' phase boundary at high temperatures but by the T_0' curve at low temperatures.

It is assumed that the supersaturation in the ferrite is constant for any given isothermal transformation temperature. On the other hand, there is no reason why the supersaturation should not decrease continuously towards equilibrium as the fraction of transformation increases at a constant temperature. This simply does not happen, e.g. we do not see martensite evolving into Widmanstätten ferrite. In other words, the models are theoretically elegant but do not reflect reality.

6.9   Cooperative Growth of Ferrite and Cementite

Ferrite and cementite grow together with a common transformation front during the formation of a pearlite colony. Hultgren (1947) proposed that the essential difference between pearlite and bainite is that in the latter case the cementite and ferrite do not grow cooperatively (Fig. 6.25). The microstructural evolution illustrated is now known to be incorrect, but it is nevertheless often argued that bainite is simply the product of a non-lamellar eutectoid reaction in which the component phases no longer share a common front with the austenite. This is doubtful for a variety of reasons, one of which is that bainitic ferrite can form without any carbide precipitation at all.

There have been attempts to revitalise Hultgren's ideas by adopting a generalised definition of bainite as the product of a non-lamellar, noncooperative
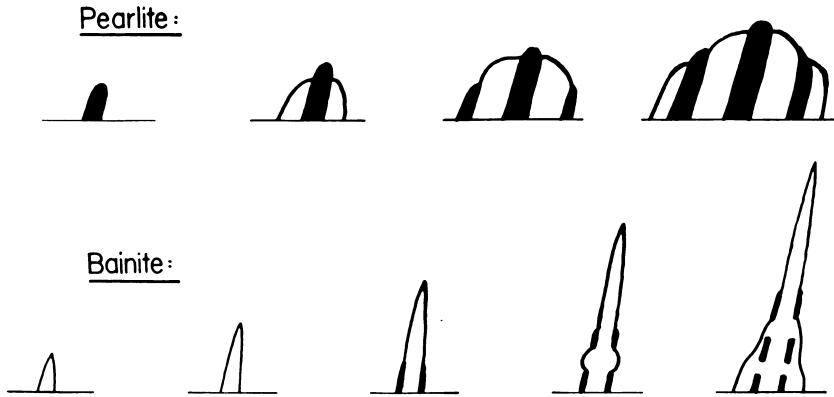
161

Pearlite:

Bainite:

Fig. 6.25 Hultgren's interpretation of the cooperative and noncooperative growth modes of pearlite and bainite respectively.

mode of eutectoid decomposition. It is further assumed that both pearlite and bainite grow by a reconstructive mechanism in which the transformation front propagates by a ledge mechanism (Lee *et al.*, 1988). It is then claimed that the transition from pearlite to bainite occurs when the cementite and ferrite can no longer grow at the same rate from austenite. The ferrite and cementite cease to grow at the same rate when:

$$\frac{h_\alpha}{\lambda_\alpha} \neq \frac{h_\theta}{\lambda_\theta} \tag{6.41}$$

where h and λ represent the height and interledge spacing respectively. The phases can grow with a common front as long as this ratio is identical for both. The ledges are supposed to move in a direction parallel to the transformation front. They are therefore shared, i.e., they can traverse both ferrite and cementite. Cooperative growth fails when:

$$\frac{h_\alpha v_\alpha^s}{\lambda_\alpha} \neq \frac{h_\theta v_\theta^s}{\lambda_\theta} \tag{6.42}$$

where v^s is the step velocity. The ledge velocity must change when it moves from the ferrite to the cementite phase to account for the change in the phases which are in local equilibrium, but this is neglected in the analysis.

It is doubtful whether this criterion identifies the essential difference between bainite and pearlite. The character of the transformation interface, whether it is glissile or sessile, is not a part of the analysis.

162

6.10 Overall Transformation Kinetics

6.10.1 Isothermal Transformation

A model for a single transformation begins with the calculation of the nucleation and growth rates, but an estimation of the volume fraction requires impingement between particles to be taken into account. This is generally done using the extended volume concept of Johnson, Mehl, Avrami, and Kolmogorov (Christian, 1975). Referring to Fig. 6.26, suppose that two particles exist at time t; a small interval δt later, new regions marked a, b, c & d are formed assuming that they are able to grow unrestricted in extended space whether or not the region into which they grow is already transformed. However, only those components of a, b, c & d which lie in previously untransformed matrix can contribute to a change in the real volume of the product phase (α):

$$dV^\alpha = \left(1 - \frac{V^\alpha}{V}\right)dV_e^\alpha \qquad (6.43)$$

where it is assumed that the microstructure develops randomly. The subscript e refers to extended volume, V^α is the volume of α and V is the total volume. Multiplying the change in extended volume by the probability of finding untransformed regions has the effect of excluding regions such as b, which clearly cannot contribute to the real change in volume of the product. For a random distribution of precipitated particles, this equation can easily be integrated to obtain the real volume fraction,
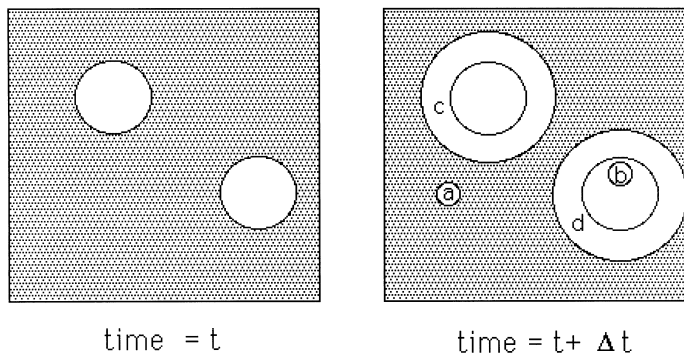

time = t   time = t+ Δt

Fig. 6.26 An illustration of the concept of extended volume. Two precipitate particles have nucleated together and grown to a finite size in the time t. New regions c and d are formed as the original particles grow, but a & b are new particles, of which b has formed in a region which is already transformed.

$$\frac{V^\alpha}{V} = 1 - \exp\left\{-\frac{V_e^\alpha}{V}\right\}$$

The extended volume V_e^α is straightforward to calculate using nucleation and growth models and neglecting completely any impingement effects. Consider a simple case where the α grows isotropically at a constant rate G and where the nucleation rate per unit volume is I_V. The volume of a particle nucleated at time τ is given by

$$v_\tau = \frac{4}{3}\pi G^3 (t - \tau)^3$$

The change in extended volume over the interval τ and $\tau + d\tau$ is

$$dV_e^\alpha = \frac{4}{3}\pi G^3 (t - \tau)^3 \times I_V \times V \times d\tau$$

On substituting into equation 6.43 and writing $\xi = V^\alpha / V$, we get

$$dV^\alpha = \left(1 - \frac{V^\alpha}{V}\right)\frac{4}{3}\pi G^3 (t - \tau)^3 I_V \, d\tau$$

so that
$$-\ln\{1 - \xi\} = \frac{4}{3}\pi G^3 I_V \int_0^t (t - \tau)^3 d\tau \qquad (6.44)$$

and
$$\xi = 1 - \exp\{-\pi G^3 I_V t^4 / 3\}$$

This equation has been derived for the specific assumptions of random nucleation, a constant nucleation rate and a constant growth rate. There are different possibilities but they often reduce to the general form:

$$\xi = 1 - \exp\{-k_A t^n\} \qquad (6.45)$$

where k_A and n characterise the reaction as a function of time, temperature and other variables. This equation is frequently used empirically as an economic way of representing experimental data (Radcliffe *et al.*, 1963; Okamoto and Oka, 1986). The temptation to deduce mechanistic information from an empirical application of the Avrami equation should be avoided even when the equation accurately fits the data, since the fitting parameters can be ambiguous.

6.10.2 Mechanistic Formulation of the Avarmi Equation

Reasonable trends can be obtained using an Avrami model founded on the mechanism of the bainite (Singh, 1998). Each nucleus is assumed to transform into one sub-unit of bainite of volume u. The time required to nucleate is considered to be much greater than that for growth so that the change in extended volume over the interval τ and $\tau + d\tau$ is given by

164

$$dV_e^\alpha = I_V V u \, d\tau$$

If ξ is defined as a normalised fraction of bainite, i.e. the fraction of bainite divided by its maximum fraction:

$$\xi = \frac{V^\alpha}{V} \bigg/ V_{max} \qquad \text{where} \qquad V_{max} \simeq \frac{x_{T_0'} - \bar{x}}{x_{T_0'} - x^{\alpha\gamma}}$$

then the conversion from extended to real volume becomes

$$dV^\alpha = (1 - \xi)dV_e^\alpha$$
$$= (1 - \xi)VuI_V \, d\tau \qquad (6.46)$$
$$\text{or} \quad V_{max}d\xi = (1 - \xi)uI_V \, d\tau$$

For every successful nucleation event, a further number p of nucleation sites is introduced autocatalytically. It follows that over a period τ there will be $pI_V\tau$ new nucleation sites introduced in addition to those originally present. The total number density N_V^T of sites at time τ therefore becomes

$$N_V^T = N_V^0 + pI_V\tau$$

where N_V^0 is the initial number density[†]. The nucleation rate (equation 6.15) therefore becomes time-dependent:

$$I_V = N_V^0\nu \exp\left\{ -\frac{G^*}{RT} \right\} + N_V^0\nu^2\tau p \exp\left\{ -\frac{2G^*}{RT} \right\}$$

On substitution into equation 6.46 we get

$$\frac{V_{max}}{uN_V^0\nu} \int_0^\xi \frac{d\xi}{\exp\{-\frac{G^*}{RT}\}} = \int_0^t \left[1 + p\tau\nu \exp\left\{ -\frac{G^*}{RT} \right\} \right]$$

which after integration and manipulation gives the time t to achieve a specified amount of transformation as:

$$t = \frac{-1 + \sqrt{1 - \frac{V_{max}}{uN_V^0}p\ln\{1 - \xi\}}}{p\nu \exp\{-\frac{G^*}{RT}\}} \qquad (6.47)$$

Some example calculations are shown in Fig. 6.27 which illustrates the advantages of formulating the Avrami theory on the basis of transformation mechan-

---

[†]Tzeng (2000) has attempted to introduce autocatalysis differently, by considering nucleation at the bainite/austenite surface. However, his mathematical derivations are wrong because his model is formulated to allow nucleation on *extended area* rather than real area. This is why his calculation of the bainite/austenite surface per unit volume tends to infinity. Similarly, w in his equations is an extended volume which should not be multiplied by I_0.
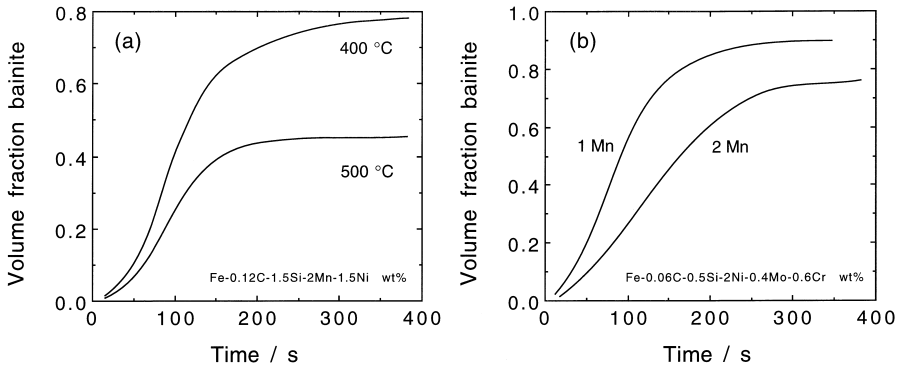
Fig. 6.27 The calculated influence of (a) transformation temperature and (b) manganese concentration on the kinetics of the bainite reaction (Singh, 1998).

ism. The maximum fraction decreases as the transformation temperature is raised towards the B_S temperature, consistent with the incomplete transformation phenomenon. Similarly an increase in the stability of the austenite (change in manganese) retards transformation.

6.10.3   *Austenite Grain Size Effect*

The bainite transformation is much less sensitive to the austenite grain size than is pearlite (Umemoto *et al.*, 1980). Furthermore, elements like boron, which increase the hardenability by segregating to the grain boundaries, have a much smaller effect on bainite than on ferrite. This is because for each bainite plate nucleated at a grain surface, there are a number which are autocatalytically stimulated; the majority of plates in a sheaf do not touch the austenite grain boundaries.

A reduction in the austenite grain size should, nevertheless, lead to an increase in the rate of transformation because of the greater number density of grain boundary nucleation sites (Barford and Owen, 1961). However, Davenport (1941) argued that the grain size has no appreciable effect on the transformation kinetics. By contrast, Graham and Axon (1959) suggested that because the growth of a bainite plate is resisted by the matrix, a smaller grain size should retard growth.

The austenite grain size is best defined by its mean line lineal intercept $\overline{L}$ because it is related inversely to the grain surface per unit volume S_V and hence to the number density of nucleation sites N_V^0:

$$S_V = \frac{2}{\overline{L}} \qquad \text{and therefore,} \qquad N_V^0 \propto \frac{1}{\overline{L}} \qquad (6.48)$$

166

It follows that the nucleation rate must increase as the austenite grain size decreases. If this is the only effect then the overall rate of transformation must increase as $\overline{L}$ decreases.

There is, however, another effect since the maximum volume V_{max}^S of a sheaf which starts from each grain boundary nucleus must be constrained by the grain size, i.e.

$$V_{max}^S \propto \overline{L}^3$$

If this effect is dominant then the overall rate will decrease as the austenite grain size is reduced. Thus, it has been demonstrated experimentally that there is an acceleration of transformation rate as $\overline{L}$ is reduced when the overall
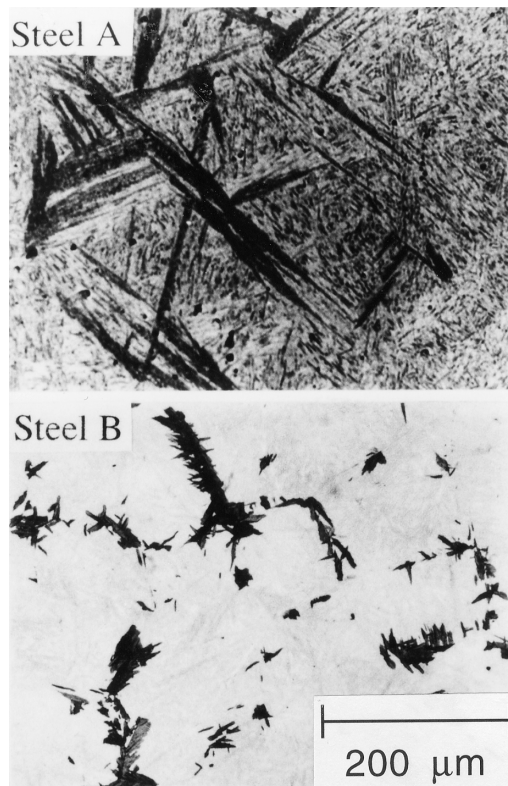

Fig. 6.28 (a) Bainite in a steel where nucleation is sparse and sheaf-growth is rapid. The austenite grains constrain the amount of transformation that each nucleus can cause. Reducing the austenite grain size then causes a net reduction in the overall rate of transformation. (b) Bainite in a steel where the growth rate is small so that the effect of the austenite grain size is simply to promote the nucleation rate. After Matsuzaki and Bhadeshia (1999).

reaction is limited by a slow growth rate, i.e. when the sheaf volume remains smaller than V^S_{max} and hence is unconstrained by the grain size. Conversely, for rapid growth from a limited number of nucleation sites, a reduction in the austenite grain size reduces the total volume transformed per nucleus and hence retards the overall reaction rate. The two circumstances are illustrated in Fig. 6.28.

6.10.4 Anisothermal Transformation Kinetics

A popular method of converting between isothermal and anisothermal transformation data is the *additive reaction rule* of Scheil (1935). A cooling curve is treated as a combination of a sufficiently large number of isothermal reaction steps. Referring to Fig. 6.29, a fraction $\xi = 0.05$ of transformation is achieved during continuous cooling when

$$\sum_i \frac{\Delta t_i}{t_i} = 1 \tag{6.49}$$

with the summation beginning as soon as the parent phase cools below the equilibrium temperature.

The rule can be justified if the reaction rate depends solely on ξ and T. Although this is unlikely, there are many examples where the rule has been empirically applied to bainite with success (e.g. Umemoto *et al.*, 1982). Reactions for which the additivity rule is justified are called isokinetic, implying that the fraction transformed at any temperature depends only on time and a single function of temperature (Avrami, 1939; Cahn, 1956).
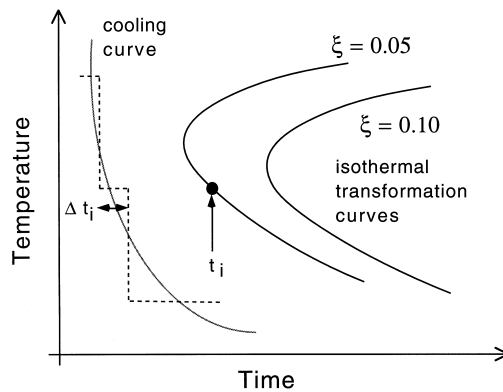

Fig. 6.29 The Scheil method for converting between isothermal and anisothermal transformation data.

6.11 Simultaneous Transformations

A simple modification for two precipitates (α and β) is that equation 6.43 becomes a coupled set of two equations,

$$dV^\alpha = \left(1 - \frac{V^\alpha + V^\beta}{V}\right)dV_e^\alpha \qquad \text{and} \qquad dV^\beta = \left(1 - \frac{V^\alpha + V^\beta}{V}\right)dV_e^\beta \quad (6.50)$$

This can be done for any number of reactions happening together (Robson and Bhadeshia, 1997; Jones and Bhadeshia, 1997). The resulting set of equations must in general be solved numerically, although a few analytical solutions are possible for special cases which we shall now illustrate (Kasuya *et al.*, 1999).

6.11.1 Special Cases

For the simultaneous formation of two phases whose extended volumes are related linearly:

$$V_e^\beta = BV_e^\alpha + C \qquad \text{with} \qquad B \geq 0 \qquad \text{and} \qquad C \geq 0 \qquad (6.51)$$

then with $\xi_i = V_i/V$, it can be shown that

$$\xi^\alpha = \int \exp\left\{-\frac{(1 + B)V_e^\alpha + C}{V}\right\}\frac{dV_e^\alpha}{V} \qquad \text{and} \qquad \xi^\beta = B\xi^\alpha \qquad (6.52)$$

If the isotropic growth rate of phase α is G and if all particles of α start growth at time $t = 0$ from a fixed number of sites N_V per unit volume then $V_e^\alpha = N_V \frac{4\pi}{3}G^3t^3$. On substitution of the extended volume in equation 6.52 gives

$$\xi^\alpha = \frac{1}{1 + B}\exp\left\{-\frac{C}{V}\right\}\left[1 - \exp\left\{-\frac{(1 + B)N_V\frac{4\pi}{3}G^3t^3}{V}\right\}\right] \quad \text{with} \quad \xi^\beta = B\xi^\alpha$$

$$(6.53)$$

The term $\exp\{-C/V\}$ is the fraction of parent phase available for transformation at $t = 0$; it arises because $1 - \exp\{-C/V\}$ of β exists prior to commencement of the simultaneous reaction at $t = 0$. Thus, ξ^β is the additional fraction of β that forms during simultaneous reaction. It is emphasised that $C \geq 0$. A case for which $C = 0$ and $B = 8$ is illustrated in Fig. 6.30.

For the case where the extended volumes are related parabolically (Kasuya *et al.*, 1999):
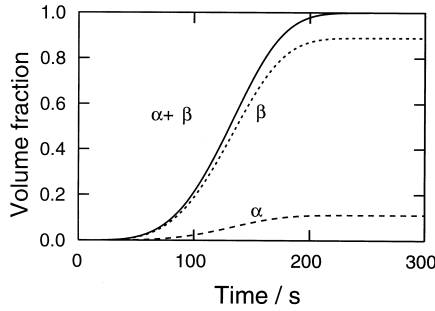
169

Fig. 6.30 Simultaneous transformation to phases $\alpha \equiv 1$ and $\beta \equiv 2$ with $C = 0$ and $B = 8$.

$$\xi^{\alpha} = \exp\left\{ -\frac{C}{V} \right\} \left[\sqrt{\frac{\pi}{4A}} \exp\left\{ \frac{(1+B)^2}{4A} \right\} \left(\text{erf}\left\{ \frac{1+B}{\sqrt{4A}} + \sqrt{A}V_e^{\alpha} \right\} \right. \right.$$

$$\left. \left. - \text{erf}\left\{ \frac{1+B}{\sqrt{4A}} \right\} \right) \right] \qquad (6.54)$$

$$\xi^{\beta} = \exp\left\{ -\frac{C}{V} \right\} \left[1 - \exp\left\{ -\frac{A(V_e^{\alpha})^2 + (1+B)V_e^{\alpha}}{V} \right\} \right] - \xi^{\alpha}$$

The volume fractions ξ^i again refer to the phases that form *simultaneously* and hence there is a scaling factor $\exp\{-C/V\}$ which is the fraction of parent phase available for coupled transformation to α and β.

6.11.2 *Precipitation in Secondary Hardening Steels*

Whereas the analytical cases described above are revealing, it is unlikely in practice for the phases to be related in the way described. This is illustrated for secondary hardening bainitic and martensitic steels of the kind used commonly in the construction of power plant. The phases interfere with each other not only by reducing the volume available for transformation, but also by removing solute from the matrix and thereby changing its composition. This change in matrix composition affects the growth and nucleation rates of all the participating phases.

The calculations must allow for the simultaneous precipitation of M_2X, $M_{23}C_6$, M_7C_3, M_6C and Laves phase. M_3C is assumed to nucleate instantaneously with the paraequilibrium composition. Subsequent enrichment of M_3C as it approaches its equilibrium composition is accounted for. All the phases, except M_3C, are assumed to form with compositions close to equili-

brium. The driving forces and compositions of the precipitating phases are calculated using standard thermodynamic methods.

The interaction between the precipitating phases is accounted for by considering the change in the average solute level in the matrix as each phase forms. This is frequently called the *mean field approximation*. It is necessary because the locations of precipitates are not predetermined in the calculations.

A plot showing the predicted variation of volume fraction of each precipitate as a function of time at 600 °C is shown in Fig. 4.16. It is worth emphasising that there is no prior knowledge of the actual sequence of precipitation, since all phases are assumed to form at the same time, albeit with different precipitation kinetics. The fitting parameters common to all the steels are the site densities and interfacial energy terms for each phase. The illustrated dissolution of metastable precipitates is a natural consequence of changes in the matrix chemical composition as the equilibrium state is approached.

Consistent with experiments, the precipitation kinetics of $M_{23}C_6$ are predicted to be much slower in the 2.25Cr1Mo steel compared to the 10CrMoV and 3Cr1.5Mo alloys. One contributing factor is that in the 2.25Cr1Mo steel a relatively large volume fraction of M_2X and M_7C_3 form prior to $M_{23}C_6$. These deplete the matrix and therefore suppress $M_{23}C_6$ precipitation. The volume fraction of M_2X which forms in the 10CrMoV steel is relatively small, so there remains a considerable excess of solute in the matrix, allowing $M_{23}C_6$ to precipitate rapidly. Similarly, in the 3Cr1.5Mo steel the volume fractions of M_2X and M_7C_3 are insufficient to suppress $M_{23}C_6$ precipitation to the same extent as in the 2.25Cr1Mo steel.

It is even possible in this scheme to treat precipitates nucleated at grain boundaries separately from those nucleated at dislocations, by taking them to be different phases in the sense that the activation energies for nucleation will be different.

6.11.3   *Time-Temperature-Transformation (TTT) Diagrams*

Transformation curves on TTT diagrams tend to have a C shape because reaction rates are slow both at high and at low temperatures. The diffusion of atoms becomes difficult at low temperatures whereas the driving force for transformation is reduced as the temperature is raised. The phase diagram thus sets the thermodynamic limits to the decomposition of austenite (Fig. 6.31).

Most TTT diagrams can be considered to consist essentially of two C curves, one for high temperatures representing reconstructive transformations to ferrite or pearlite. The other is for the lower temperatures where substitutional atoms take too long to diffuse, so that reconstructive transformations are replaced by displacive transformations such as Widmanstätten ferrite and
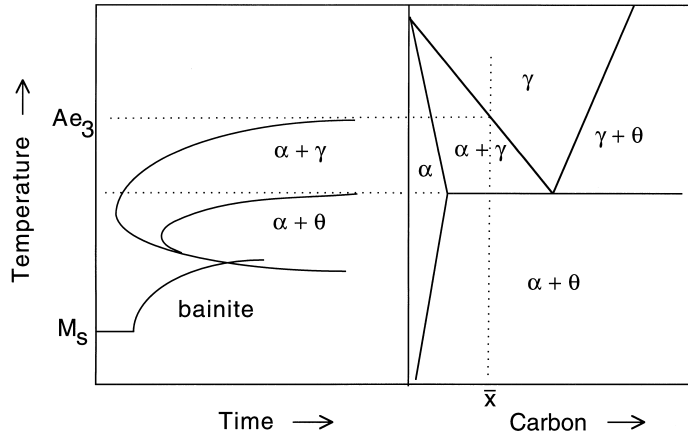
171

Fig. 6.31 The relationship between a TTT diagram for a hypoeutectoid steel with a concentration $\bar{x}$ of carbon, and the corresponding Fe-C phase diagram.

bainite. The martensite-start temperature generally features on a TTT diagram as a horizontal line parallel to the time axis (Cohen, 1940).

There are two major effects of alloying additions on transformation kinetics. Solutes which decrease the driving force for the decomposition of austenite retard the rate of transformation and cause both of the C curves to be displaced to longer times. At the same time they depress the martensite-start temperature (Fig. 6.32). The retardation is always more pronounced for reconstructive reactions where all atoms have to diffuse over distances comparable to the size of the transformation product. This diffusional drag exaggerates the effect of solutes on the upper C curve relative to the lower C curve.

For steels where the reaction rate is rapid, it becomes difficult experimentally to distinguish the two C curves as separate entities. For plain carbon and very low-alloy steels, the measured diagrams take the form of just a single C curve over the entire transformation temperature range. This is because the different reactions overlap so much that they cannot easily be distinguished using conventional experimental techniques (Hume-Rothery, 1966). Careful experiments have shown this interpretation to be correct (Brown and Mack, 1973; Kennon and Kaye, 1982). Sometimes the degree of overlap between the different transformation products decreases as the volume fraction of transformation increases (Fig. 6.33). This is because the partitioning of solute into austenite has a larger effect on reconstructive transformations.

As predicted by Zener (1946), when the two curves can be distinguished clearly, the lower C curve has a flat top. This can be identified with the Widmanstätten ferrite-start or bainite-start temperature, whichever is the larger in magnitude (Bhadeshia, 1981a).
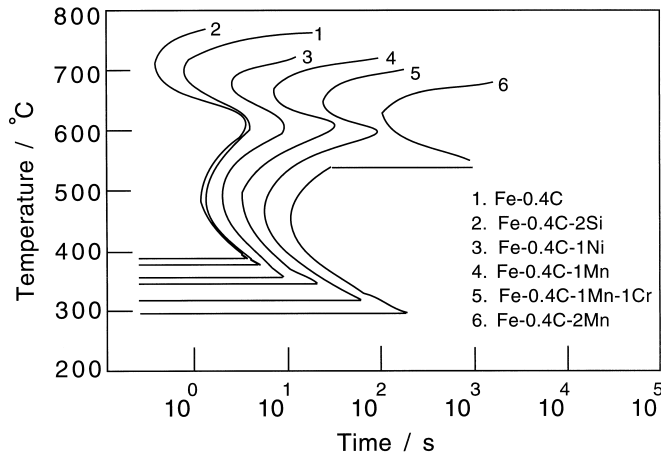
172

Fig. 6.32 Calculated TTT diagrams showing the C-curves for the initiation of reactions for a variety of steels.
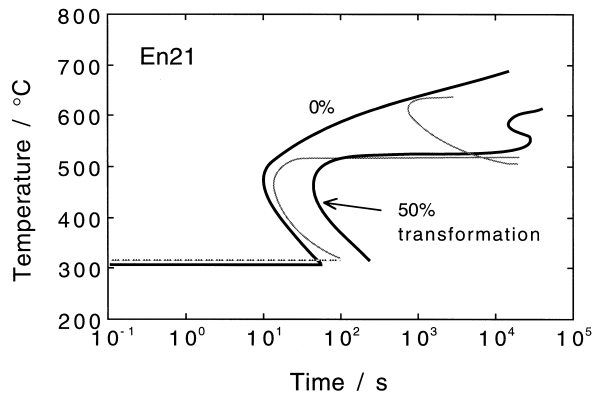

Fig. 6.33 TTT diagram for Steel En21 (BISRA, 1956). The continuous lines are experimental. The separation of the two constituent C curves, which is not apparent for the 0% curve is revealed as the extent of reaction increases. The dashed curves are calculated for 0% transformation.

There is more detail than implied in the two C curve description. The upper and lower bainite reactions can be separated on TTT diagrams (Schaaber, 1955; White and Owen, 1961; Barford, 1966; Kennon, 1978; Bhadeshia and Edmonds, 1979a). There is even an acceleration of the rate of isothermal transformation just above the classical M_S temperature, due to the formation of isothermal

173

martensite (Howard and Cohen, 1948; Schaaber, 1955; Radcliffe and Rollason, 1959; Smith *et al.*, 1959; Brown and Mack, 1973a,b; Babu *et al.*, 1976; Oka and Okamoto, 1986, 1988).

Isothermal martensite plates tend to be very thin and are readily distinguished from bainite. Although the overall rate of martensitic transformation appears isothermal, the individual plates are known to grow extremely rapidly. The isothermal appearance of the overall reaction is therefore due to the nucleation process (Smith *et al.*, 1959). The stresses caused by bainitic transformation seem to trigger induced isothermal martensite. The rate eventually decreases as the transformation temperature is reduced below the M_S temperature, giving the appearance of a C-curve with the peak transformation rate located below M_S (Fig. 6.34).

6.11.4 Continuous Cooling Transformation (CCT) Diagrams

Steels are not usually isothermally transformed. It is more convenient to generate the required properties during continuous cooling from the austenitic
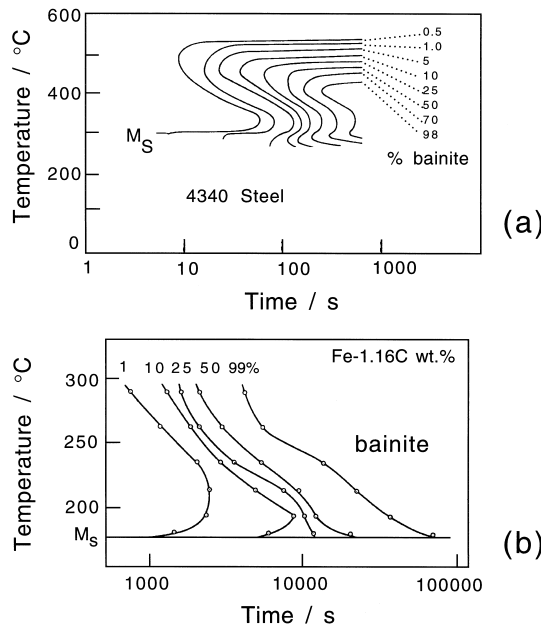

Fig. 6.34 (a) TTT diagram for a Fe–0.39C–0.70Mn–1.7Ni–0.76Cr–0.2Mo–0.28Si–0.22Cu wt% alloy austenitised at 900 °C for 15 minutes. Note the acceleration in the rate of transformation as the M_S temperature is approached (data from Babu *et al.*, 1976). (b) Similar data for a plain carbon steel (Howard and Cohen, 1948).

174

condition. Continuous-cooling-transformation (CCT) diagrams are then used to represent the evolution of microstructure (Fig. 6.35).

The rate of transformation in a given steel with a known austenite grain size can be described with just one TTT diagram. However, a different CCT diagram is required for cooling function, e.g. whether the cooling rate is constant or Newtonian. It is therefore necessary to plot the actual cooling curves used in the derivation of the CCT diagram (Fig. 6.35). Each cooling curve must begin at the highest temperature where transformation becomes possible (usually the Ae_3 temperature).

Each CCT diagram requires a specification of the chemical composition of the steel, the austenitisation conditions, the austenite grain size and the cooling condition. The diagrams are therefore specific to particular processes and lack the generality of TTT diagrams.

The CCT diagram is usually partitioned into domains of microstructure; Fig. 6.35 shows the conditions under which bainite and ferrite form. Mixed microstructures are obtained when a domain boundary is intersected by a cooling curve. The constant volume fraction contours must be continuous across the domain boundaries to avoid (incorrect) sudden changes in volume fraction as the boundary is crossed (e.g. points *a, b* on Fig. 6.36). The contours represent the fraction of austenite which has transformed into one or more phases. It follows that there are constraints on how the zero percent martensite and bainite curves meet, avoiding the double intersection with the cooling curve illustrated in Fig. 6.36b,c. Cooling curve *X* which leads to a fully martensitic
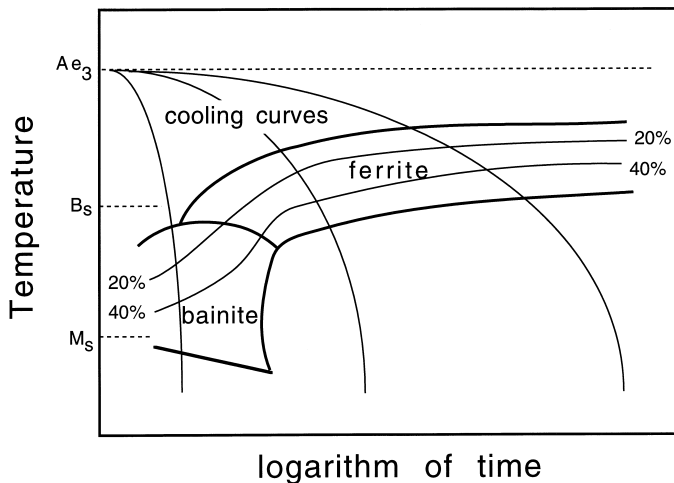

Fig. 35 CCT diagram illustrating the cooling curves, constant volume percent contours and transformation temperatures.
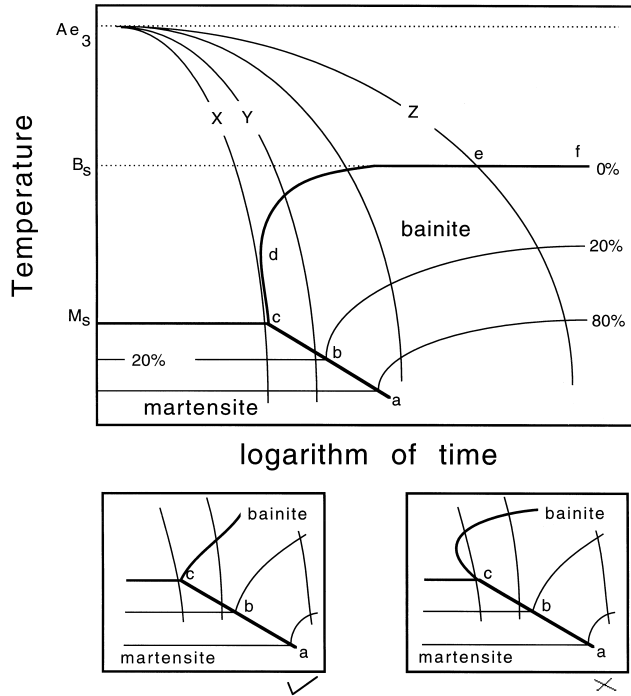
175

Fig. 6.36 Schematic CCT diagrams illustrating the continuity of constant volume percent contours across microstructure domain boundaries and the correct way in which the zero percent curves of different domains must meet at the point *c*.

microstructure, intersects the 0% transformation curve at just one point, without intersecting the region *cd*. Cooling curve *Y*, on the other hand, produces a mixed microstructure with less than 20% of bainite, the remaining austenite transforming to martensite on cooling. The temperature at which martensitic transformation begins (line *abc*) is depressed if bainite forms first and enriches the residual austenite with carbon.

The bainite curve in Fig. 6.36 approaches the B_S temperature asymptotically along *ef* as the cooling rate decreases consistent with the flat top of the bainite C curve in the TTT diagram. This is not always the case as shown schematically in Fig. 6.37. (Kunitake, 1971; Schanck, 1969; Lundin *et al.*, 1982). Any transformation which precedes bainite alters the chemical composition of the residual austenite. The main changes occur in the region associated with the vertical line 'c' in Fig. 6.37 The temperature at which the bainite first forms is depressed by the changed composition of the austenite. Because the ferrite and bainite domains are separated by a time gap, the continuity of constant volume fraction contours is interrupted. The contours must still be plotted so that
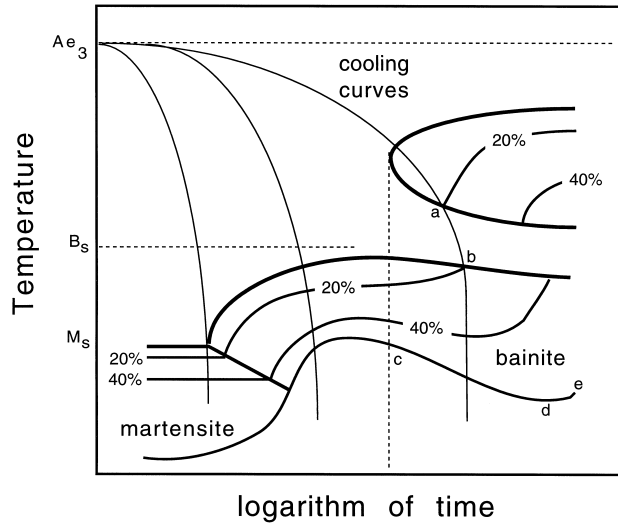
176

Fig. 6.37 TTT diagram in which the bainite region is strongly influenced by the initial formation of ferrite during continuous cooling transformation.

their loose ends are connected by a cooling curve as illustrated by 'ab' on Fig. 6.37.

Although bainite is depressed to lower temperatures by the prior formation of allotriomorphic ferrite as the cooling rate decreases, the temperature range over which bainite forms is eventually reduced. This is because very slow cooling rates give ample opportunity for transformation to be completed over a smaller temperature range as illustrated by the rising curve 'de' on Fig. 6.37.

All of the features described here can be found in actual TTT and CCT diagrams, for example, the measured diagrams for a '2.25Cr1Mo' steel which is used widely in the bainitic condition for power plant applications (Fig. 6.38).

6.11.5   Boron, Sulphur and the Rare Earth Elements

The early commercial development of bainitic steels relied on the effect of boron on the transformation characteristics of low-carbon steels (Chapter 1). Boron retards the heterogeneous nucleation of allotriomorphic ferrite at the austenite grain surfaces, to a greater degree than that of bainite (Fig. 6.39). This in turn permits boron-containing steels to be cooled continuously into fully bainitic microstructures. Elements like manganese are not suitable because they improve the martensite hardenability and hence favour a mixed microstructure of bainite and martensite.
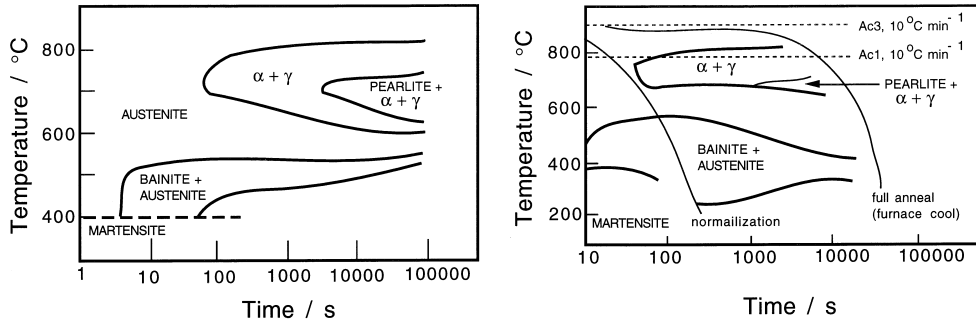
177

Fig. 6.38 Corresponding TTT and CCT diagrams for a 2.25Cr1Mo steel (Lundin *et al.*, 1982). The CCT diagram shows the terminology used in describing air-cooling from the austenitisation temperature (i.e., normalising) and furnace cooling (i.e. annealing).
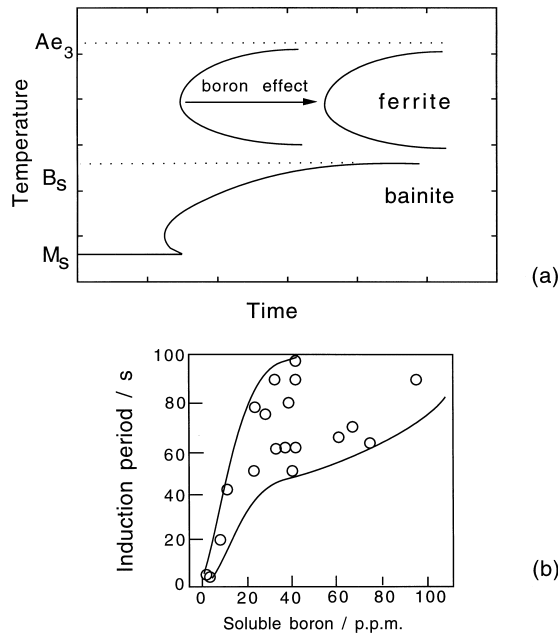

Fig. 6.39 (a) The effect of boron and its analogues (the rare earth elements) on the TTT diagram. There is a pronounced effect on the allotriomorphic ferrite transformation but only a minor retardation of bainitic reaction. (b) Change in the incubation time for the allotriomorphic ferrite reaction as a function of the soluble boron concentration. (After Pickering, 1978).

178

Boron segregates to austenite grain boundaries. In doing so it reduces the grain boundary energy and hence makes the boundaries less effective as heterogeneous nucleation sites. A typical boron addition of $\simeq 0.002$ wt% is sufficient to have a profound effect on transformation kinetics, although the exact amount must clearly depend on the austenite grain size. Too much boron precipitates as borides which stimulate the nucleation of ferrite. The boron is only effective in enhancing hardenability when present in solid solution, not when precipitated as oxides or nitrides (Fig. 6.40). It is for this reason that boron containing steels are usually deoxidised with aluminium. Titanium is added to tie up any nitrogen which may otherwise combine with the boron and render it impotent.

Carbon also tends to segregate to austenite grain boundaries. In low carbon steels, niobium or titanium forms carbides thereby reducing the quantity available for segregation. This leaves the boundaries open to receive boron (Tamehiro *et al.*, 1987a,b). Otherwise the boron can be displaced from the grain boundaries by the preferential segregation of carbon.

The efficacy of boron is influenced by the presence of nonmetallic inclusions, especially in steel welds or in inoculated steels where inclusions are added deliberately to induce the precipitation of desirable forms of bainite. For example, MnS and Al_2O_3 particles seem to act as heterogeneous nucleation sites for BN and $M_{23}C_6$ during fabrication (Saeki *et al.*, 1986). This reduces the free boron available for segregation to the ferrite nucleation sites (Dionne *et al.*, 1988).

Quite small concentrations of sulphur ($\simeq 0.005$ wt%) can sometimes stimulate the nucleation of bainite (Umemoto *et al.*, 1986b). Iron-rich sulphides precipitate at the austenite grain boundaries and form potent sites for the nucleation of bainite.
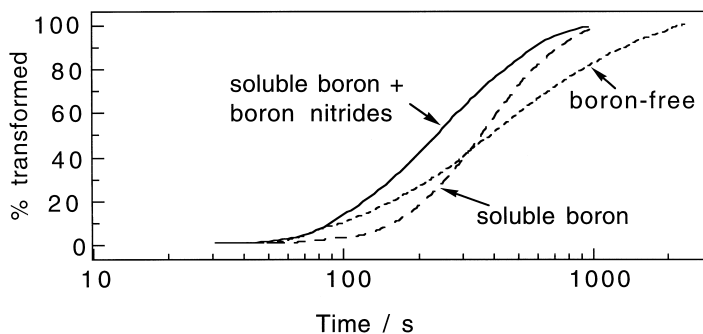

Fig. 6.40 Experimental data due to Ueda *et al.* (1980) for three steels. The rate of reaction is slow in the sample containing soluble boron and fast in the one containing boron nitride, compared with the boron-free steel.

179

Rare-earth elements including cerium, neodymium, lanthanum and yttrium are believed to act in a manner similar to boron (Jingsheng *et al.*, 1988). Attention has been focused on cerium additions of up to 0.134 wt%, where it is found that allotriomorphic ferrite formation is retarded relative to that of bainite. The mechanism is said to involve the segregation of cerium to the austenite grain boundaries. The effect of cerium is dramatically reduced if the phosphorous content exceeds $\simeq 0.02$ wt%, although the mechanism of this interaction is not yet established.

An indirect role of elements such as yttrium comes from their ability to getter sulphur, especially in the presence of sulphides which influence the nucleation frequency of ferrite (Abson, 1987).

6.12 Superhardenability

Transformations in a moderately hardenable steel can be retarded by super-heating the melt to about 1650 °C during steelmaking, as long as the aluminium concentration is in the range 0.03–0.05 wt% (Brown and James, 1980). This phenomenon is dubbed the *superhardenability effect*; the effect on TTT diagrams is shown in Fig. 6.41.

The effect is most pronounced with high hardenability steels; it is also enhanced by increasing the aluminium concentration to about 0.06 wt% before it saturates (Mostert and van Rooyen, 1982). Superhardenability is not influenced by prolonged holding at the austenitisation temperature, as sometimes happens with hardenability increments due to boron additions. Some of the samples used in the original experiments were cast in air, the others in argon, and tests were carried out for both superheated (1650 °C) and conventional melts (1550 °C), at varying concentrations of aluminium. The superheated melts were held at 1650 °C for a few minutes and then cooled to 1550 °C, where alloying additions were made before casting.

The superheat apparently causes the breakdown of clusters of alloying atoms in the liquid and this influences hardenability (Sachs *et al.*, 1980). This fails to explain why holding a superheated melt at a lower temperature before casting does not reform the clusters and hence eliminate the superhardenability. Furthermore, superheating is not necessary when the melting is carried out under an inert atmosphere.

An alternative interpretation is based on nonmetallic inclusions such as manganese oxysulphides or titanium oxides in the steel. These can help nucleate ferrite and so reduce hardenability (Chapter 10). Aluminium is a stronger oxidising element than Mn, Si, or Ti. It forms alumina which is ineffective as a heterogeneous nucleation site for ferrite. The preferential formation of alumina would therefore lead to an increase in hardenability. This hypothesis explains several features of the superhardenability effect:
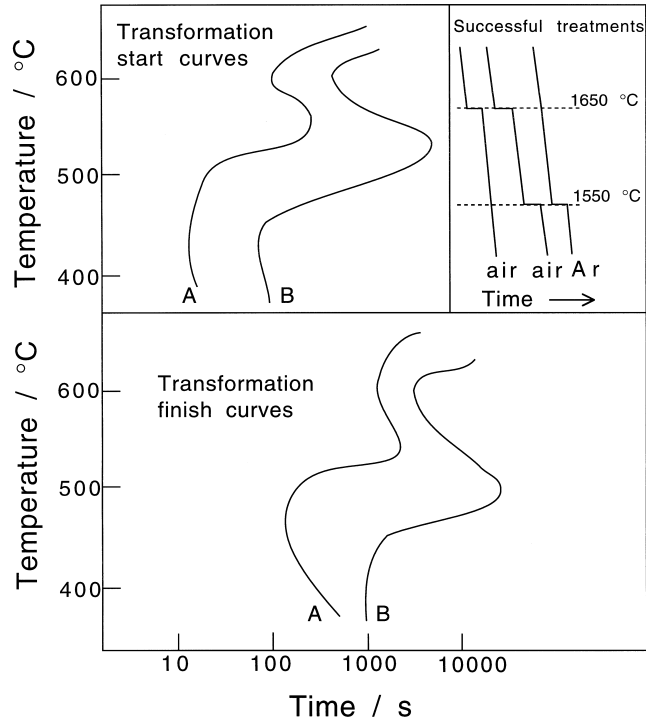
180

Fig. 6.41 The superhardenability effect. Curves *A* and *B* represent steels which were cast using melt temperatures of 1550 and 1650 °C respectively. The steels have similar compositions but their aluminium concentrations are 0.03 and 0.09 wt% respectively. After Mostert and van Rooyen (1982).

(i) The need to add aluminium.

(ii) That superheat is not needed when an inert gas cover is used during steelmaking. This would lead to a reduction in the oxygen concentration and hence the number density of the oxide nucleation sites.

(iii) Consistent with experimental data, an inclusion effect should not fade during prolonged austenitisation.

(iv) The additional nucleation sites on inclusions can only contribute significantly in steels which already have a reasonable hardenability, i.e. where any enhancement of nucleation kinetics would have a noticeable outcome.

The potent influence of inclusions is well established in welding metallurgy (Chapter 10). Controlled experiments are now needed, in which the trace element concentrations (Al, Ti, O, N, S, B) are carefully monitored.

6.13 The Effect of Chemical Segregation

Commercial steels do not have a uniform chemical composition. The thermo-mechanical processing used in the manufacturing process improves matters but the final product still is heterogeneous. Solute segregation can have a profound effect on the development of microstructure, for example, in the development of bands of transformation products (Fig. 6.42). The segregation structure of solidification is spread out into bands parallel to the rolling plane during deformation. The microstructural bands follow the segregation pattern because it is the local chemical composition that determines the onset of transformation.

The scale of segregation compares with the spacing of the secondary dendrite arms of the solidification microstructure, with a repeat distance of a few tens of micrometers. The peak concentrations are about factor of two of the mean values. Any coherency strains caused by variations in lattice parameter due to these composition gradients can therefore be neglected. Such strains become important in the theory of spinodal decomposition (or artificial multi-layered structures) where the gradients are much larger.

It is the segregation of substitutional solutes which is the real cause of banding. Carbon diffuses rapidly and becomes homogeneous in the austenite; there may be small concentration variations as the carbon attempts to achieve a uniform chemical potential in the presence of substitutional solute gradients (Kirkaldy *et al.*, 1962).
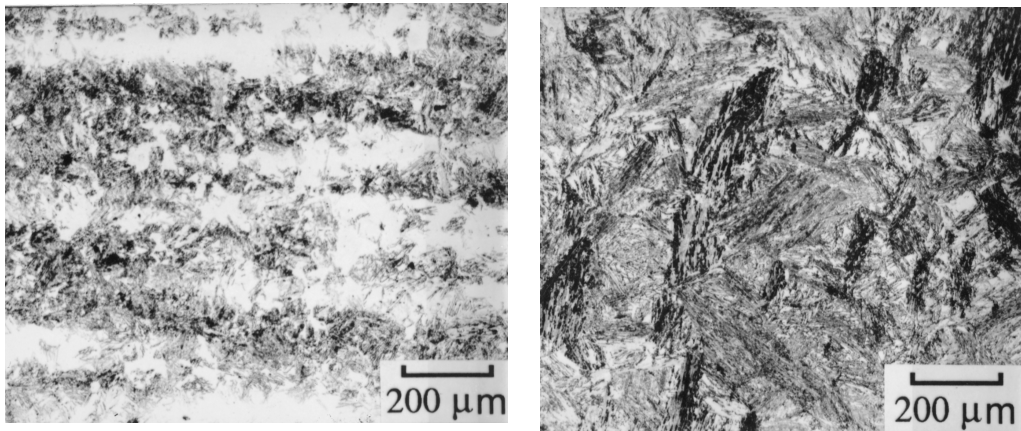

Fig. 6.42 (a) Optical micrograph illustrating the banded microstructure obtained in a heterogeneous steel (300M) after isothermal transformation to bainite; (b) corresponding optical micrograph for the sample which was homogenised prior to isothermal transformation to bainite (Khan and Bhadeshia, 1990a).

182

Although carbon is homogeneously distributed in the austenite, the preferential formation of ferrite in the substitutional-solute depleted regions causes a partitioning of carbon into the adjacent substitutionally-enriched regions. The resulting carbon-enriched bands have a profound influence on the development of microstructure, but it is important to realise that the redistribution of carbon is a consequence of solid state transformation and only indirectly due to the solidification process.

Davenport (1939) compared the isothermal transformation kinetics of steels containing banding with those which had been homogenised by annealing in the austenitic condition. It is expected that transformation should start first in the solute-depleted regions, and at a temperature which is higher than that for a homogenised steel. The early part of the TTT diagram of segregated steels is expected to reflect the behaviour of the solute-depleted regions. Conversely, the C curves for the later stages of transformation should reflect slower transformations in the solute-enriched regions. Davenport's experiments did confirm this; the C curves for the initiation of bainite in the segregated steels were frequently found to be at longer times when compared with homogenised steels.

The observations are summarised in Fig. 6.43. The reaction is faster in the heterogeneous sample at high transformation temperatures, but not as the undercooling below the B_S temperature increases. The rate is always found to be slower in the heterogeneous samples when considering the later stages of transformation. Experiments by Grange (1971) are consistent with these observations. The fact that the C curves of the homogeneous and heterogeneous
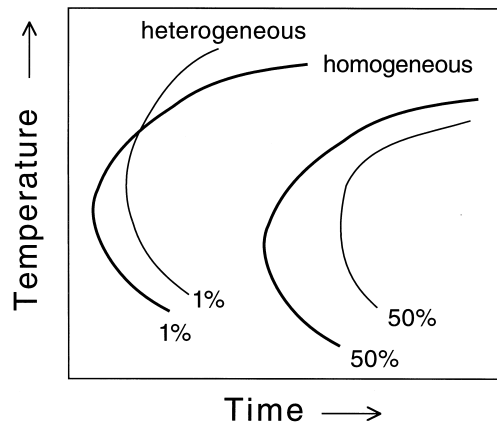

Fig. 6.43 The effect of chemical segregation on the bainite C curves of TTT diagrams.

183

samples cross is difficult to understand if it is argued that transformation should always be easier in the solute-depleted regions.

The peculiar behaviour illustrated in Fig. 6.43 has been explained quantitatively (Khan and Bhadeshia, 1990a). The segregated steel is able to transform in its solute-depleted regions at temperatures above B_S for the homogeneous alloy. This advantage is maintained at small undercoolings. However, at higher undercoolings the homogeneous steel is able to transform faster because bainite can nucleate uniformly in all regions, whereas it is only able to form in the depleted regions of the heterogeneous alloy.

The carbon partitioned during transformation is localised near the platelets so on a coarser scale it is more uniformly distributed in the homogeneous sample where the bainite grows everywhere. By contrast, most of the partitioned carbon remains in the substitutional solute depleted regions of the segregated sample and retards the development of transformation. The effect is prominent at large undercoolings because the maximum fraction of bainite that can form is greater. Anything which enables the distribution of carbon to become more uniform gives heterogeneous steels a kinetic advantage. For example, slow cooling through the transformation range (Fig. 6.44).

To summarise, when bainite forms during continuous cooling transformation, the reaction may begin at a higher temperature in segregated steels, but both the extent and rate of subsequent transformation should be larger in homogenised alloys.
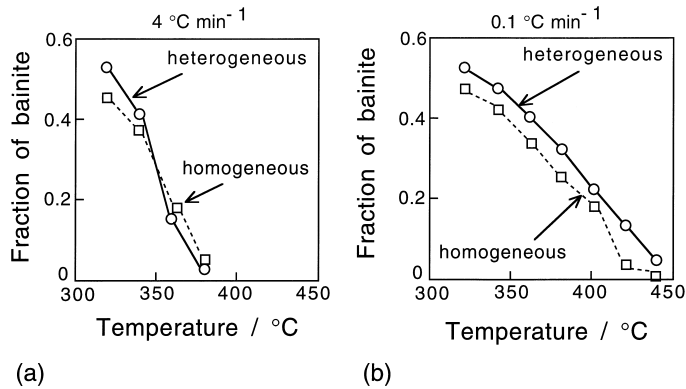

(a)   (b)

Fig. 6.44 Experiments on homogenised and heterogeneous steel samples in which bainitic transformation was obtained by continuous cooling: (a) $4\,°C\,min^{-1}$; (b) $0.1\,°C\,min^{-1}$. The slower cooling conditions permit a more uniform distribution of carbon in the residual austenite, in which case the heterogeneous sample transforms to a greater extent relative to the homogenised sample, at all temperatures.

6.14 Martensitic Transformation in Partially Bainitic Steels

The formation of bainite enriches the residual austenite and introduces strains and defect. This must influence the way in which the residual austenite transforms subsequently to martensite.

The progress of the athermal martensitic transformation is usually described empirically using the Koistinen and Marburger (1959) equation:

$$1 - \xi = \exp\{-C_6(M_S - T_Q)\} \tag{6.55}$$

where ξ is the volume fraction of martensite, T_Q is a temperature to which the sample is cooled below M_S and $C_6 \simeq 0.011\,\mathrm{K}^{-1}$ is a constant obtained originally by fitting to experimental data.

Magee (1970) justified this equation by assuming that the number density of new plates of martensite per unit volume of austenite, dN, is proportional to the change in the driving force $\Delta G^{\gamma\alpha}$ on cooling below M_S:

$$dN = -C_7 d(\Delta G^{\gamma\alpha})$$

where C_7 is a proportionality constant. The change in the volume fraction of martensite is therefore given by:

$$d\xi = \overline{V} dN_V$$

where dN_V is the change in the number of new plates of martensite formed per unit volume of sample, given by $dN_V = (1 - \xi)dN$. On combining these equations and substituting $[d(\Delta G^{\gamma\alpha})/dT]dT$ for $d(\Delta G^{\gamma\alpha})$ we get:

$$d\xi = -\overline{V}(1 - \xi)C_7 \frac{d(\Delta G^{\gamma\alpha})}{dT} dT$$

which on integration between the limits M_S and T_Q gives

$$\ln\{1 - \xi\} = \overline{V}C_2 \frac{d(\Delta G^{\gamma\alpha})}{dT}(M_S - T_Q)$$

or

$$1 - \xi = \exp\left\{\overline{V}C_2 \frac{d(\Delta G^{\gamma\alpha})}{dT}(M_S - T_Q)\right\} \tag{6.56}$$

which has a similar form as the equation used by Koistinen and Marburger.

6.41.1 Autocatalysis

The initial number density N_i^0 of the defects responsible for the nucleation of martensite is not large enough to explain the observed rate of martensitic

transformation (Shih *et al.*, 1955; Pati and Cohen, 1951; Olson and Cohen, 1981). The extra defects necessary to account for the shortfall are obtained by *auto-catalysis*. Each plate of martensite creates new embryos in the austenite. Their number density is given by integrating (Lin, 1987):

$$dN = dN_i + d(\xi p)$$

where N_i is the number density of original nucleation sites which survive at any stage of transformation:

$$N_i = (1 - \xi)N_i^0 p \tag{6.57}$$

where p is number of autocatalytic sites generated per unit volume of sample, assumed to be related linearly to the volume fraction of martensite and hence to ξ,

$$p = C_8 + C_9\xi$$

so that $\quad dN = (-N_i^0 + C_8 + 2C_9\xi)d\xi$

Since $\overline{V}$ is assumed to be constant,

$$d\xi/\overline{V} = (1 - \xi)dN$$

so that

$$\int \frac{d\xi}{\overline{V}(1 - \xi)} = \int (-N_i^0 + C_3 + 2C_4\xi)d\xi. \tag{6.58}$$

Integration gives

$$p = N_i^0 - \frac{\ln\{1 - \xi\}}{\xi\overline{V}} \tag{6.59}$$

It is found experimentally that:

$$p - N_i^0 = C_{10} + C_{11}(M_S - T_Q)$$

On setting $M_S - T_Q = 0$, it is found that $C_{10} = 1/\overline{V}$. It follows that

$$-\frac{\ln\{1 - \xi\}}{\xi} = 1 + \overline{V}C_6(M_S - T_Q) \equiv 1 + C_{12}(M_S - T_Q) \tag{6.60}$$

This is an alternative kinetic model for the development of martensitic trans-formation as a function of undercooling below the M_S temperature. It has been used to rationalise martensite transformation kinetics in fully austenitic sam-ples as well as those which are first partially transformed to bainite.

Although a reasonable fit has been demonstrated (Fig. 6.45), the model tends to overestimate the fraction transformed when the amount of martensite is small.
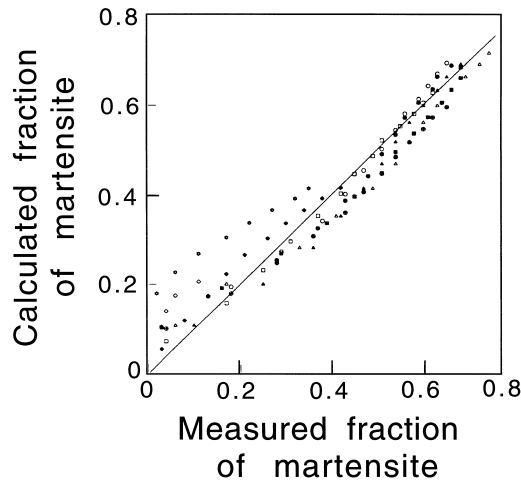
Fig. 6.45 Comparison of experimental results with those calculated by fitting equation 6.60 to the experimental data. After Khan and Bhadeshia, 1990b.

6.15   Summary

Both the individual platelets and the sheaves of bainite lengthen at rates much faster than permitted by the diffusion of carbon. It must be concluded that they grow with a supersaturation of carbon, the ferrite inheriting the composition of the parent austenite. The excess carbon is soon afterwards partitioned into the residual austenite or precipitates as carbides.

It is possible that not all the carbon is trapped in the ferrite during transformation. However, neither the experimental evidence nor the theory for growth with partial supersaturation is convincing.

Carbon must partition during the nucleation of bainite. The nucleation probably occurs by a displacive mechanism akin to martensite, but with the most potent sites confined to the austenite grain surfaces. Autocatalytic nucleation plays a role but it is not as prominent for bainite as it is for martensite. The activation energy for nucleation varies linearly with the driving force. Nucleation does not therefore rely on heterophase fluctuations, but rather on the dissociation of dislocation clusters. The activation energy is in these circumstances from the resistance to interfacial motion.

The calculation of overall transformation kinetics remains challenging. Whereas some important trends are reproduced, accurate predictions using few parameters are not yet possible. This indicates that important variables remain to be identified. A qualitative result is that bainitic transformation is less sensitive to the austenite grain size when compared with pearlite. This is

because sheaf growth occurs by the propagation of sub-units at sites away from the austenite grain surfaces.

Except at temperatures close to B_S, homogeneous steels transform more rapidly than those containing chemical segregation. The martensitic decomposition of austenite left untransformed after the growth of bainite can be described adequately by the theory for the martensitic decomposition of fully austenitic samples.